EFFECTIVE SURFACE AREAS AND ADSORPTION CAPACITY OF GRAPHENE WITH VACANCIES

A DISSERTATION IN
Physics
and
Electrical and Computer Engineering

Presented to the Faculty of the University of
Missouri–Kansas City in partial fulfillment
of the requirements for the degree

DOCTOR OF PHILOSOPHY

by

JONATHAN LEE

B.S., University of Miami, Coral Gables, FL, 2015
M.S., University of Missouri Kansas City, Kansas City, MO, 2018

Kansas City, Missouri
2023

EFFECTIVE SURFACE AREAS AND ADSORPTION CAPACITY OF GRAPHENE WITH VACANCIES

Jonathan Lee, Candidate for the Doctor of Philosophy Degree
University of Missouri–Kansas City, 2023

ABSTRACT

Graphene has been heavily researched since Geim and Novosolov won the nobel prize in physics for its mechanical exfoliation from graphite.[1] The atomically thin crystal of carbon atoms has been reported to have novel properties across varied metrics.[2] One such metric is the incredibly high specific surface area of $2360 m^2 g^{-1}$. Literature has advised the employment of graphene with vacancy defects for applications such as sensors, separation, supercapacitors, and batteries.[3–6]

Pores have been put into devices for these applications, yet the effects of vacancies in graphene require more study to be fully understood.[3] An alarming discrepancy exists between the theoretical and experimental determination of

graphene's specific surface area. It is proposed here that experimental samples may contain vacancy defects, leading to an overestimation of specific surface area.

Presented here is both an analytical discussion and a molecular dynamics based approach of evaluating the effects of pore size and pore geometry on potential energy, adsorption capacity calculation and effective specific surface area. It is determined that a single vacancy defect can lead to an increase (~300 $m^2 g^{-1}$) in specific surface area as well as adsorption capacity. 73% of this increase is shown to be due to an increase in adsorption in a conical volume around the introduced pore.

APPROVAL PAGE

The faculty listed below, appointed by the Dean of the School of Graduate Studies, have examined a dissertation titled "Effective Surface Areas and Adsorption Capacity of Graphene with Vacancies," presented by Jonathan Lee, candidate for the Doctor of Philosophy degree, and hereby certify that in their opinion it is worthy of acceptance.

Supervisory Committee

_____

Da-Ming Zhu, Ph.D., Committee Chair
School of Science and Engineering

Paul Rulis, Ph.D.
School of Science and Engineering

Elizabeth Stoddard, Ph.D.
School of Science and Engineering

Mahbube Siddiki, Ph.D.
School of Science and Engineering

Mostafizur Rahman, Ph.D.
School of Science and Engineering

CONTENTS

ILLUSTRATIONS

Figure Page

TABLES

Table Page

ACKNOWLEDGEMENTS

First, I would like to thank Dr. Da-Ming Zhu for his continuous guidance and support throughout my graduate studies and research. His help has been invaluable as my research advisor and the chair of my committee. I would also like to express my gratitude to my supervisory committee. I appreciate the time and effort spent reviewing my dissertation.

I would like to thank my family for providing me with a support system that I am lucky to have. This work would not have been possible without the assistance of the people listed here. For this, I am sincerely grateful.

CHAPTER 1

INTRODUCTION

1.1 Historical Context

Graphene is an atomically thin, hexagonal crystal of carbon atoms. It is a singular, planar layer of the more commonly known graphite. Graphene's identification awarded Andre Geim and Konstantin Novoselov the 2010 Nobel Prize in physics for their 2004 paper on atomically thin carbon films.[1] This paper however, was not the earliest consideration of graphene.

In 1859, the chemist Benjamin Brodie exposed graphite to strong acids and produced what he called "carbonic acid".[7] This process is now known to produce a suspension of graphene oxide crystals, which are graphene layers chemically bonded to groups of hydroxyl, hydrogen-oxygen, and epoxide, carbon-oxygen-carbon.[8]

In 1948, Ruess and Vogt dried a droplet of the graphene-oxide suspension and viewed it with transmission electron microscopy. They observed crumpled flakes of graphene-oxide that were a few nm thick. [9] In 1961, Hofmann and Boehm's group employed this approach with the goal of finding the thinnest fragment of reduced graphene-oxide. Reduced means that some of the hydroxy and epoxide groups are removed from the graphene plane through thermal,

chemical, or photo-thermal treatment. Hofmann and Boehm identified some reduced graphene oxide flakes as monolayers.[10] This could be considered as the first identification of graphene, though Hofmann and Boehm expressed doubt due to the potential unintended carbon coatings in their transmission electron microscope or defects in the reduced graphene-oxide layer.

In 1986 Boehm et al. introduced the name graphene as a combination of 'graphite' and the suffix '-ene' applied to fused polycyclic aromatic hydrocarbons.[11] Fused polycyclic aromatics are compounds built from multiple cyclic rings such as the hexagon of carbon atoms in Benzene, C_6H_6. Boehm's paper discusses the recommended terminology surrounding graphite intercalation compounds. Intercalation refers to the introduction of heteroatoms between graphite planes that do not destroy their planarity. It was suggested that individual carbon layers in graphite intercalation compounds should be referred to as graphene.

In the decades following Boehm et al.'s name introduction, groups were able to produce graphene layers on metal[12], graphite[13] and silicon carbide[14] substrates with epitaxial growth methods. Epitaxial growth refers to crystal

growth upon an oriented film or substrate. Atoms are obtained for deposition via the decomposition of chemical precursors or laser ablation.

In the early 2000s there were reports of single, scrolled up layers of graphene. Groups used a process of intercalating graphite layers with potassium to produce the intercalation compound KC_8. The layers were chemically exfoliated with ethanol- potassium chemical reactions at intercalation layers to create a dispersion of graphene sheets.[15] [16] The sheets would tend to curl upon themselves to form scrolls.

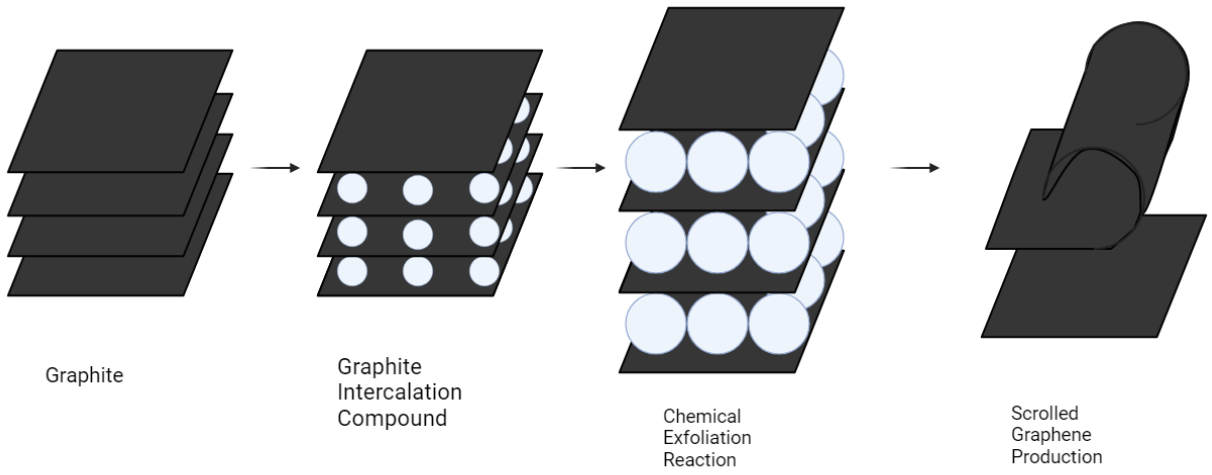

Figure 1 Chemical Exfoliation Schematic

In 2004 Geim and Novosalev used a mechanical exfoliation approach to generate free standing planar few-layer graphene as well as monolayer graphene. The supporting material of their publication details the process. The group began with 1 mm thick highly oriented pyrolytic graphite and used

oxygen plasma etching to create 5-micron thick plateaus. The plateaus were transferred to a layer of wet photoresist where the group used tape to repeatedly cleave off layers of graphite. In doing so, graphene flakes would land into the wet photoresist and would be released by acetone treatment. Silicon wafers were dipped into the solution and washed with propanol and water. Washing removed thick flakes while the thinner, < 10 nm, ones remained on the wafer's surface. Optical, electron beam and atomic force microscopes were then used to verify the quality of the graphene flakes. [1] The reliable production of single graphene planes led to a boom in the material's research.[17]

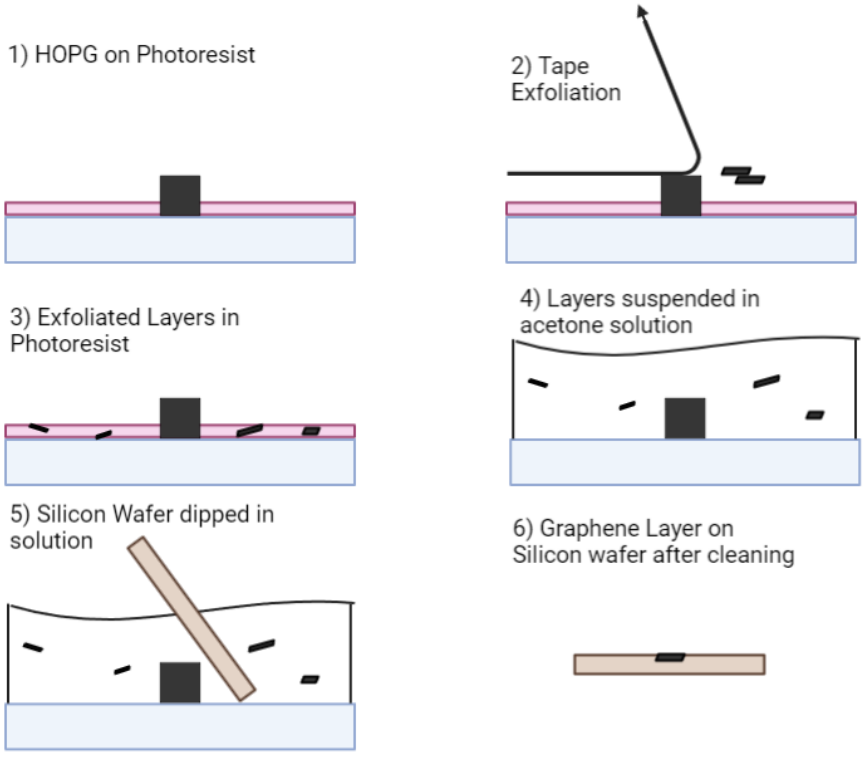

Figure 2 Mechanical Exfoliation Schematic

1.2 Purpose

This dissertation presents background information about topics of carbon allotropes, adsorption, interatomic potentials and nanoporous graphene. Literature relevant to nanoporous graphene fabrication, applications, and challenges are presented and reviewed.

This work proposes a resolution to the discrepancy posed in literature between the theoretically and experimentally determined values of Graphene's specific surface area. Experimental overview and results will produce information about potential energy curves, adsorption capacity and specific surface area of ideal graphene and nanoporous graphene.

1.3 Contributions

The major contributions of this dissertation can be summarized as follows. Presented here is both an analytical discussion and a molecular dynamics-based approach of evaluating the effects of pore size and pore geometry on potential energy, adsorption capacity and effective specific surface area of porous graphene. It is determined that single vacancy defects can lead to a dramatic increase in specific surface area as well as adsorption capacity. The volume in which an increase of specific surface area due to vacancy introduction is localized.

1.4 Outline

This dissertation is structured as follows. Chapter 1 as an introduction contains a historical context section, the purpose of the dissertation, the contributions of the work and this outline. Chapter 2 provides necessary background information about carbon allotropes, graphene structure and graphene defects. Chapter 3 summarizes the literature on nanoporous graphene fabrication, applications and their challenges. Chapter 4 introduces the proposed resolution to a problem found in literature along with an experimental overview. Chapter 5 discusses an analytical approach to calculating effective surface area changes based on pore introduction. Chapter 6 presents molecular dynamics experimental results and analysis. Finally, Chapter 7 summarizes the current work, conclusions and provides potential future directions.

CHAPTER 2

BACKGROUND INFORMATION

Geim and Novosalev showed in 2004 that a graphene plane could freely exist and produced it through what was dubbed the "tape method." Graphene itself is a carbon allotrope. Allotropes are differing structures and formations of a single element, in these cases carbon. Chemically, allotropes are the same, but the structural differences allow for vastly different physical properties. Allotropes are interesting as the structure determines the various properties of the material. Interestingly, Carbon has the highest number of identified allotropes.

2.1 Carbon Based Allotropes

Carbon is the sixth element on the periodic table, with 6 protons and 6 electrons in its charge neutral state. Carbon has four valence electrons, allowing for it to create four covalent bonds. The way these bonds form with nearby atoms define the structure of the allotropes.

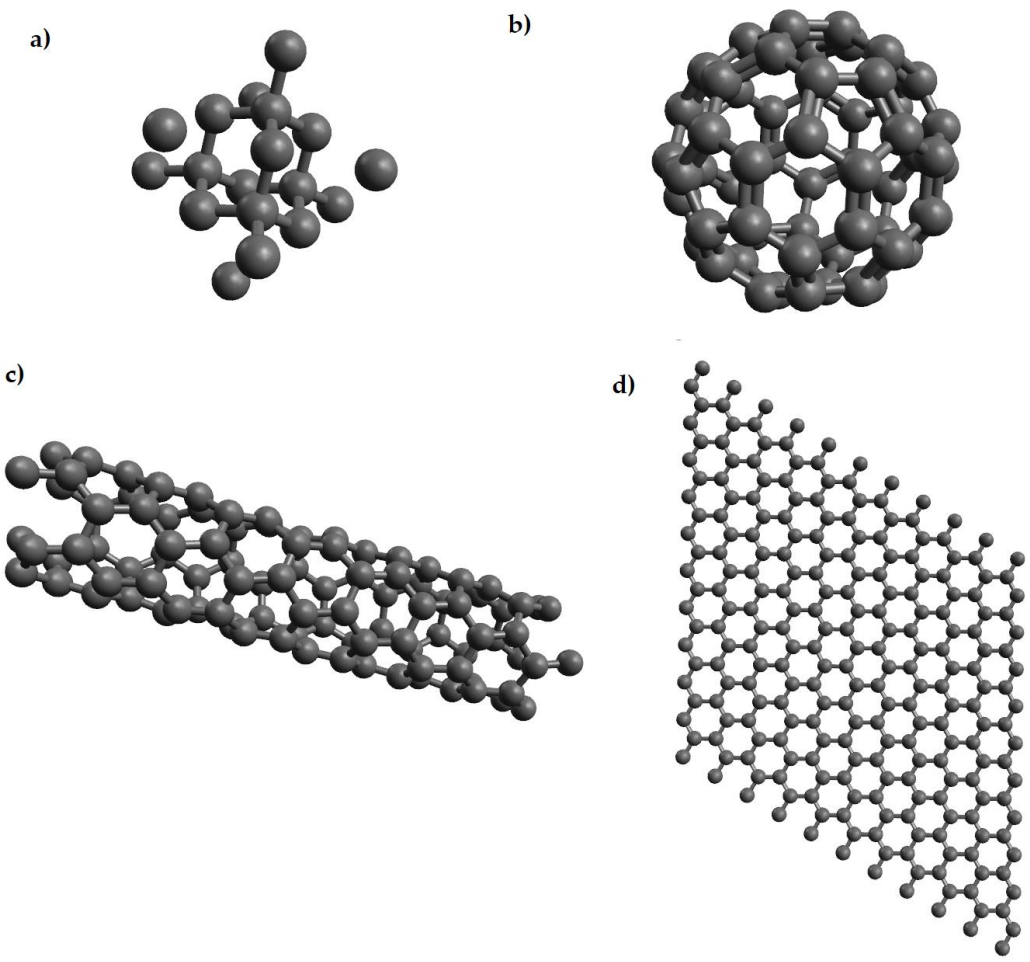

Figure 3 Structure of Carbon-Based allotropes. a) Diamond, b) C60 Buckminsterfullerene, c) Carbon Nanotube and d) Graphene

2.1.1 Amorphous Carbon

Amorphous Carbon is a structure where there is no repetition in the position of carbon atoms. This form is seen in coal, activated carbon and biochar. Activated Carbon finds use due to its surface functionality. AC has a high surface

area to volume ratio which is particularly useful in adsorbents. Due to this usefulness, activated carbon has been used as air and water purifiers. In the human body, it has been used as an adsorbent to help in poisoning cases as well as to reduce cholesterol and internal gas.[18]

2.1.2 Diamond

Diamond is a crystalline structure that is comprised of a tetrahedral cubic unit cell of space group 227. Diamond is an interesting case as it is a strong thermal conductor while being an electrical insulator. Diamonds have a use case for industrial applications such as cutting and grinding. A similar allotrope named Lonsdaleite has been predicted to have a higher material strength than diamonds. [19]

2.1.3 Graphite

Graphite is an allotrope of carbon where numerous flat structures are stacked upon each other. This allotrope, as opposed to diamond, is a great electrical conductor. The mechanism behind this difference is the bonding structure of the allotropes. Electrons in graphite exist in three σ-bonds with the three nearest neighbors and a delocalized π-bonds between carbon atom layers. Since electrons in π-bonds are less restricted to the atomic nuclei, the electrons are comparatively free to move. Diamond, however, has a restrictive bond

structure, where each carbon atom forms four single bonds with its nearest neighbors.

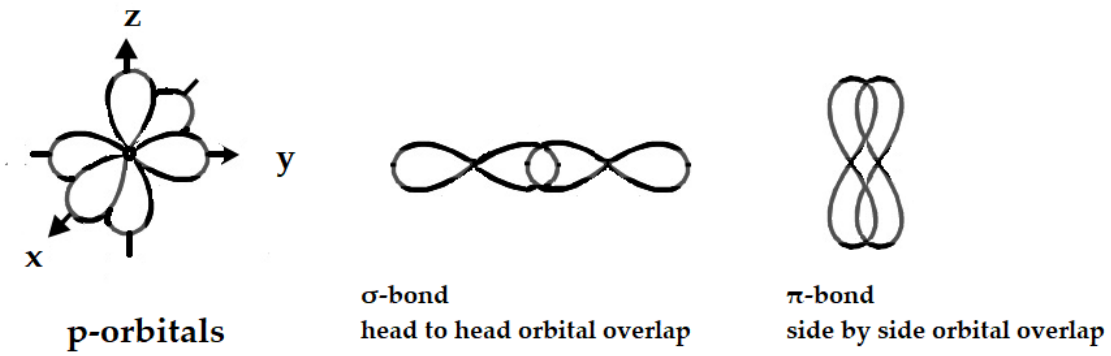

Figure 4 P-orbitals, sigma bond and pi bond layout

Layers in graphite are lightly held together with Van der Waals forces making it easy to shear layers past each other. This light attraction also allows for atoms to align themselves in between layers of graphite to generate graphite intercalation compounds. As previously mentioned, chemical exfoliation was employed to generate curved carbon nanoscrolls.[15]

2.1.4 Fullerenes

Fullerenes are defined as hollow spheres or tubes of any size composed of carbon atoms. In 1985 the C_{60} "buckeyball" fullerene was discovered by Kroto and Smalley.[20] This allotrope is a spherical molecule consisting of 60 carbon

atoms arranged into 12 pentagons and 20 hexagons. Even prior to graphene's 2004 exfoliation, carbon nanotubes (CNTs) were heavily researched in technological fields. Carbon nanotubes are nanoscale cylinders and can be single walled or multiwalled structures. In the multiwalled case, CNTs can have a minimum outer diameter of 55 Å and a minimum inner diameter of 23 Å. CNTs are interesting as they have experimentally been found to be the stiffest and strongest fibers produced. This in conjunction with their electrical properties makes CNTs a large field for application research.[18,21–23]

2.1.5 Graphene

As an isolated layer of graphite, Graphene is a planar, atomically thin, hexagonal lattice of carbon atoms. The bond distance between neighboring atoms is 1.42 Å. The atomic thickness is reported to be 3.4 Å.[2] Graphene is considered to be a basic building block for numerous graphene based structures such as multilayer graphene, graphene nanoribbons, graphene nanomesh, multi crystalline graphene and graphene oxide.

Graphene shares a bonding structure with the stacked multilayered system of graphite. Each carbon atom shares a σ-bond with the three nearest neighbors and a delocalized π-bond. π-bonds occur when there is a side-by-side overlap of p-orbitals between atoms and this occurs across the plane, allowing

for electron conduction. This bonding structure generates graphene's crystalline lattice.

Graphene's crystal structure is a hexagonal lattice of Carbon atoms. This lattice is defined by unit cell parameters that are a = 2.47 Å, b = 2.47 Å, c = 7.80 Å and α= 90° β = 90 ° γ = 120°. Basis vectors are taken as (0, 0, 1.951) and (1.234, 0.712 ,1.951). This gives each carbon-carbon bond length a value of 1.42 Å.[24]

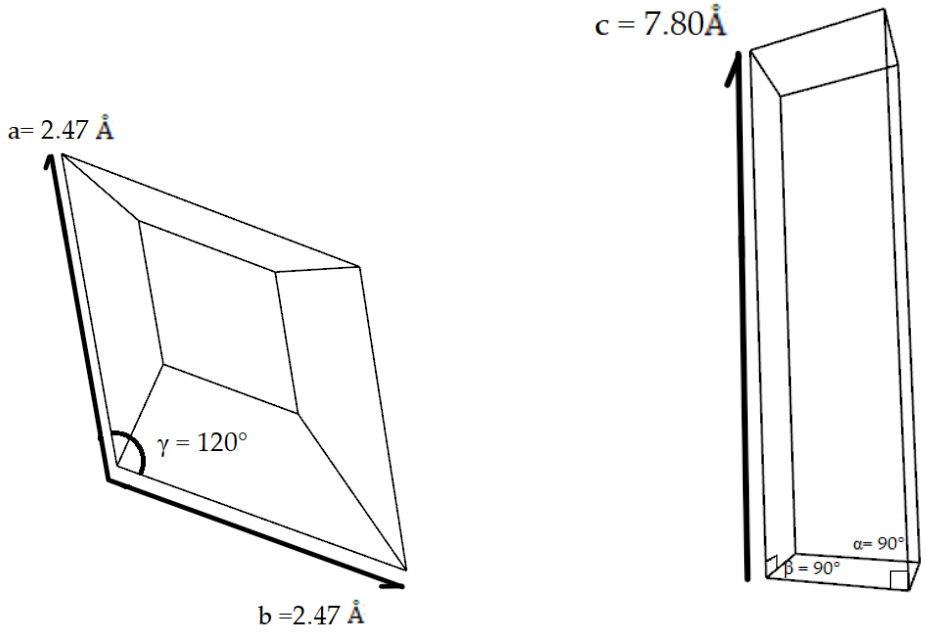

Figure 5 Graphene Unit Cell Parameters

Placing carbon atoms at the basis vector sites and replicating the unitcell creates a hexagonal lattice of carbon atoms, generating a supercell of graphene.

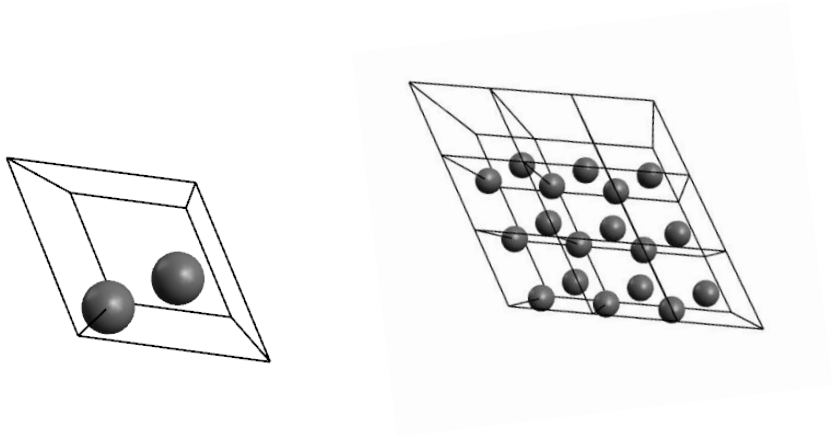

Figure 6 Graphene Basis Positions and Graphene Supercell

2.1.6 Graphene Properties

Electrons in atoms have specified energy levels, orbitals, that they can occupy. As atoms bond into molecules these orbitals overlap and the energy levels form into regions called bands. Bands naturally occupied closest to the material are called valence bands. Energetically higher bands that require excitation for electrons to reach, these are called conduction bands. Materials are classified based on their band structure. Materials with overlapping valence and conduction bands are classified as conductors. Materials with a large gap between valence and conduction bands are electrical insulators. Materials with a relatively small band gap are called semi-conductors. Graphene has a special classification as a zero-band gap semi-conductor, where certain regions of the material have overlapping valence and conduction bands.

Graphene's other impressive properties across various metrics makes it one of the most promising nanomaterials being researched. Its versatility and unique structure make it a substance of interest across varied fields. The properties that led to explosive increase in graphene research are the following: Thermal conductivity as high as 6000 W $m^{-1}\ K^{-1}$, Carrier mobility of 200,000 $cm^2 V^{-1} s^{-1}$, electrical conductivity of 3000 -5000 WmK^{-1}, Transparency of 97.7%, Young's Modulus of 1 TPa and intrinsic fracture strength of130 GPa. [25]

The property of interest for this work however is the high Specific Surface Area of 2630 $m^2\ g^{-1}$. Graphene is the only material which has every atom available for adsorption, making it a very attractive material for applications based on adsorption. Graphene is not always produced in an ideal state, there are various potential defects.

2.2 Graphene Vacancy Defects

2.2.1 Graphene Defects

Graphene produced from various fabrication methods often have defects in the graphene plane.[3,6,26] There are multiple types of possible defects including Stone-Wales defects, grain boundary defects and vacancy defects. Stone-Wales defects describe the case where nearby carbon hexagons bond instead into pairs of pentagons and heptagons.[27] Grain boundary defects occur when multiple

crystals form and grow into contact with each other, forming a misaligned boundary. Vacancy defects are the type where carbon atoms are missing from lattice sites, forming pores on a nanoscale.

Graphene surfaces with vacancy defects have some property advantages over ideal graphene. Ideal graphene's zero band gap opens and is tunable with vacancy introduction.[28] Also, the high specific surface area of graphene becomes larger with pores. A downside to vacancy defects is a reduction in mechanical strength.

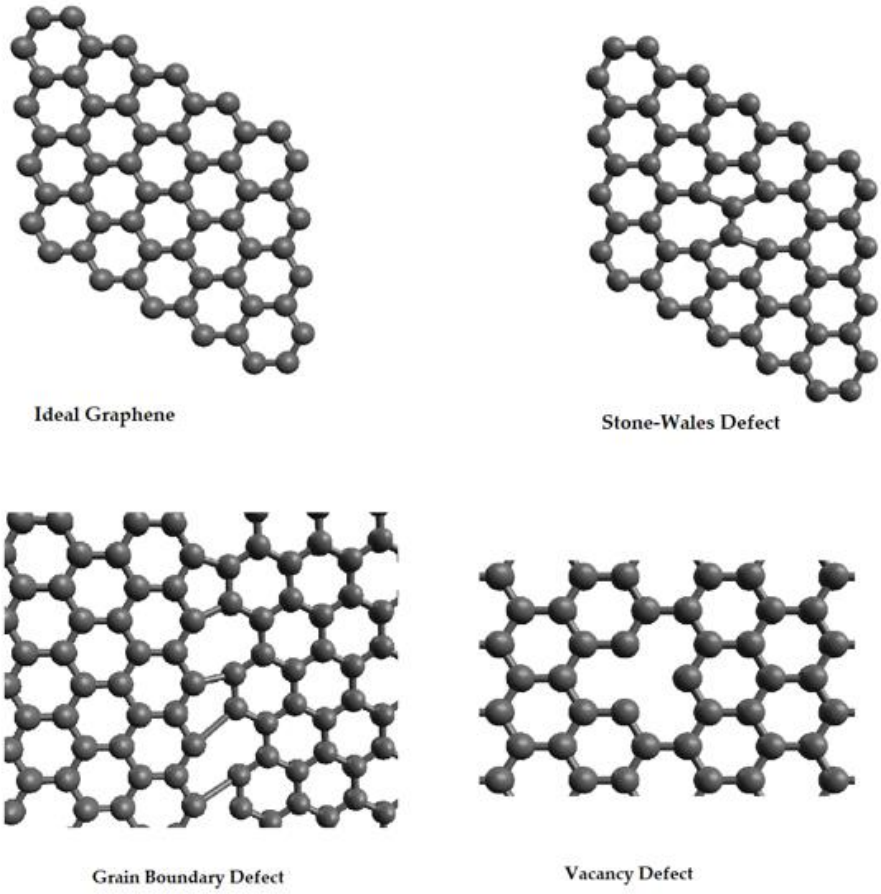

Figure 7 Ideal Graphene compared with graphene with various defect types.

CHAPTER 3

FABRICATION, APPLICATIONS AND CHALLENGES OF NANOPOROUS GRAPHENE

In this chapter, the current literature pertaining to nanoporous graphene fabrication and applications is summarized. Following this is an introduction to the discrepancy in graphene's specific surface area.

3.1 Nanoporous Graphene

Graphene with vacancy defects in the hexagonal lattice creates a structure called nanoporous graphene. Nanoporous Graphene (NPG), also referred to as graphene nanomesh or Holey graphene, is a structural derivative of graphene. Controllable nanopores allow for implementation in fields, more suitable than ideal, nonperforated graphene. Although pore generation can occur through defects in synthesis, controllable pore generation is required to control surface properties, diffusion mechanisms and to benefit from nanoscale properties. Pore sizes ranging from .15 to ~300 nm have been reported in nanoporous graphene.[3]

3.1.1 NPG Fabrication

Controlled pore generation requires specific fabrication techniques. Fabrication techniques are split into three categories: Stochastic etching, guided etching and guided growth.[3]

3.1.1.1 Guided Growth

An ideal graphene monolayer was first mechanically exfoliated from graphite in 2004 by Geim et al.[1] Since then, various other approaches have been developed to fabricate graphene. Chemical Vapor Deposition or CVD is one common method for graphene preparation. In CVD, a gaseous carbon precursor, for example methane, is placed into a heated furnace where the precursor decomposes onto a smooth substrate that is carbon inert. The carbon atoms deposited onto the substrate form the crystalline layer for graphene. A related epitaxial growth method is atomic layer deposition (ALD) where layer number is controlled.[29] Thermal reduction of graphene oxide is another popular large scale fabrication method reduced Graphene Oxide (rGO).[30]

As pertains to nanoporous graphene fabrication, guided growth employs techniques that can create pores during or after graphene nucleation. For example, CVD can be shut off at certain sites during growth to induce defects during nucleation. Templated growth, or barrier-guided CVD, is a bottom-up growth method that revolves around CVD growth around inert structures. Initially, carbon-inert templates are deposited onto a substrate, followed by graphene growth, then the template is removed. An example process by Safron et al. used block copolymers as the barriers and produced well patterned

graphene structures in micro and nano ranges.[31] Multiple domains of templated growth can be combined to create larger areas of perforated graphene. A similar process was followed by Wang et al where SiO_2 was used as the barriers.[32] Anodic Aluminium Oxide [33] and MgO[34] have also been used as barriers for templated NPG growth.

Another guided growth fabrication strategy is the use of Graphene NanoRibbons (GNRs). GNRs have been tailored into porous structures via a series of reactions leading from monomers to polymers to graphene nanoribbions to porous graphene.[35]

3.1.1.2 Guided Etching

Nanoporous graphene has been produced through lithography in processes denoted as guided etching. Guided etching from a top-down method follows general steps, initially graphene is deposited on a substrate. Then a mask or template with pores is placed above the graphene, after which a nano lithographic etching process occurs to generate pores in the graphene layer. At this point, the template is removed, leaving the porous graphene layer. Templates must be inert to graphene such that they only provide morphological guidance during etching. Various materials can serve as templates. Bai et al. used a protective layer of silicon oxide and polystyrene block copolymers with

cylindrical regions for pore production. Etching was performed with a reactive ion etch (RIE) followed by oxygen plasma etching.[36] Lee et al. used AAO as their template due to its vertical hexagonal nanochannels and wide use for nanostructure fabrication.[37] Liang et al. used polysteryne based resist coating as a template to produce nanomeshes.[28]

Sinitskii and Tour used silica nanoparticles as a template by spreading them upon graphene then partially etching it with RIE to a desired diameter of silica particles. After this an Au layer was deposited upon the stack as a protective layer, then the silica nanoparticles were removed introducing gaps in the protective layer. RIE was used again to create pores in the graphene layer and the protective layers were removed to produce porous graphene of controlled pore size.[38] The technique is known as nanosphere lithography, and can achieve highly ordered structures through the selection of nanoparticles with uniform size. Colloidal polystyrene nanoparticles serve as choices for these templates.[26]

A photolithographic and O_2 plasma etching approach was applied by Zhang et al to produce graphene meshes with pores on the tens of microns scale.[39]

Deposition of nanoparticles onto ideal graphene sheets can lead to the preparation of porous graphene. Dispersed nanoparticles can work as sites for chemical etching by serving and catalysts. This catalytic etching method also leads to less consistent hole size and regularity. Lin et al. made an example process of catalytic etching with Ag nanoparticles and thermal heated to 300 degrees C. The Ag nanoparticles were then washed away with acid wash. This produced pores, showing the catalytic role of Ag since ideal graphene wouldn't decompose at this temperature.[40] Radich et al showed a photocatalytic fabrication of porous graphene, using gold nanoparticles as catalysts. However, the gold nanoparticles in this catalytic etching process were not anchored upon the graphene sheet, meaning this is an example of stochastic etching.[41]

3.1.1.3 Stochastic Etching

Stochastic Etching differs from guided etching because it doesn't follow a template or mask. These approaches often attack intrinsic defect points from the graphene production. Thermally reduced graphene oxide creates point defects in the graphene layer. [42] Using these defect points as potential pore sites has been performed with gas-phase exfoliation. As an example, Han et al used a single step porous graphene fabrication method by heating commercial rGO to 390 degrees C.[43]

Koenig et al employed Ultraviolet oxidative etching upon mechanically exfoliated graphene that was pressurized by H_2 gas.[44] Electron beam lithography was used by Li et al to produce pores on the microscale.[22]

General interests about the above fabrication methods are production scalability, pore size, pore density, and neck width. These values impact the viability of each method as a means for production for their desired applications. Guirguis et al. have a few tables of interest linking fabrication techniques and applications.[3]

3.2 NPG Applications

3.2.1 Separation

Separation covers a broad range of nanoporous graphene applications, including gas permeation, water treatment, DNA translocation and molecular nanoseives. Graphene is an attractive material for this application due to its high mechanical strength, chemical stability and atomic thickness. Ideal graphene cannot be permeated by gasses due to the electron density. The repulsive side of the Lennard-Jones potential rejects atoms and molecules that are moving close to the graphene plane. Porous graphene, however, has pore sites where the repulsion is removed and allows for some atoms or molecules to pass through while rejecting others. This selectivity is desirable for semipermeable membranes

and separation films.[4] A 2008 publication by Sint et al. demonstrates chemically modified graphene nanopores and the ability to selectively sieve ions. The negative nitrogen and fluorine doped pores allowed cation passage and positive hydrogen doped pores allowed anion passage. Molecular dynamics simulations were used to accelerate ions with an electric field acting perpendicular to a graphene plane surrounded by water molecules. Negative Nitrogen fluorine doped pores were passed by Li+ Na+ and K+ ions and the positive Hydrogen doped pores were permeated by Cl- and Br- ions. The coulombic coupling between the doped rim of the pores and the ions allows for selective permeation due to charge and ion size.[45]

Jiang et al. computationally demonstrated porous graphene can be used to sperate molecular gasses with a selectivity much higher than commonly used polymer and silica membranes.[46] These studies showed a pore selectivity of H_2 over CH_4 which was later demonstrated experimentally by Koenig et al.[44] Liu et al used molecular dynamics to demonstrate porous graphene can selectively separate N_2 and CO_2 where the CO_2 molecules permeated pores of 3.4 angstrom size while N_2 did not.[47] Li et al performed separation tests with graphene oxide for H_2/CO_2 and H_2/N_2.[48] Huang et al showed H_2/CH_4 gas-sieving through

intrinsic defects from CVD growth and improving permeation after introducing ozone-based etching. [49]

Water treatment and desalination membranes currently are made from polymeric or inorganics such as silica, carbon and metal oxides. The issues found in present membranes are ones of low permeability and chemical stability. These issues are addressed with porous graphene due to its tunable pore size, high selectivity and high chemical stability. However, they still aren't ideal for large scale applications due to low scalability.[50] O' Hern et al combined CVD grown, intrinsically defective porous graphene film with a polycarbonate membrane to form a composite thin film. This film was able to reject 46% of potassium chloride (KCl), 71% of tetramethylammonium chloride (TMAC), 23% of), allura red AC (AR), and 17% of thiuram disulphide (TMRD) in water. These intrinsically defective structures suggest that nanoporous graphene may be used in water treatment.[51] Surwade et al demonstrated a 100% rejection of KCl using oxygen plasma etched nanoporous graphene as a desalination membrane.[52] Cohen-Tanugi and Grossman used molecular dynamics simulations and showed nanoporous graphene can filter NaCl from water.[53]

Nanoporous graphene was evaluated as a replacement for nano-porous membranes in DNA and protein translocation.[54] In a similar study graphene nanopores were evaluated for use in DNA sequencing. DNA was guided through a graphene film between two electrodes. The sequencing is done by monitoring nucleobase dependent ionic current trough the pore the chain is passing.[55,56] This particular application demonstrates NPG use in separation as well as sensing.

3.2.2 Sensors

The operational principle for nanoporous graphene sensors is to monitor electrical properties of the sensor which will vary based on the species of molecule adsorbed onto the sensor. This is demonstrated by measuring resistance changes in graphene based chemi-resistors.[57] Every atom in graphene is exposed to the environment, giving it a large sensing area and making it an attractive material for sensing applications. Porous graphene has advantages over ideal graphene by having pores that serve as energy traps and help create sites for adsorption. Zhang et al. showed higher theoretical adsorption rates for four (CO, NO, NO_2 and NH_3) small gas molecule species in defective graphene sheets over pristine sheets.[58] Paul et al. showed Field Effect Transistor (FET) based sensors with nanopores showed high sensitivity responses while those

made of pristine graphene showed no response. Here, nanosphere lithography was used to create a nanoporous graphene sensor for NO_2 and NH_3 [59]

3.2.3 Supercapacitors

Supercapacitors or ultracapacitors are energy storage devices that function by storing and releasing charge through adsorption and desorption of ions. This type of supercapacitor is known as an electrical double layer capacitor (EDLC). Supercapacitors as an energy storage device have a high power density allowing for quick discharge rates, however the energy density is low when compared to other storage devices such as batteries and fuel cells. The increase of energy density in supercapacitors is an area of interest for research. Energy stored in this type of capacitor is proportional to effective surface area. Graphene has a high effective surface area which is further increased with the introduction of pores. Furthermore, energy stored in a supercapacitor increases with voltage so the selection of electrolytes and electrodes that are stable in high voltages is ideal.

Theoretical values for nanoporous graphene electrode performance are higher than experimental values. This is due to graphene sheets restacking and preventing the full surface area to be utilized. Efforts to prevent restacking include the use of vertically oriented graphene sheets, curved graphene sheets, folded graphene sheets, crumpled graphene sheets and spacers.[60]

Experimental groups have produced nanoporous graphene electrodes with higher specific surface area than pristine graphene. Pristine graphene has a specific capacitance of 190 F/g. Liu et al used Nitrogen doped graphene in conjunction with carbon nanotubes and activated carbon to make electrode structures with improved specific capacitance of 197 F/g. [21] Kim et al used graphene nanomesh electrodes to obtain a value of 253 F/g.[6] Ning et al. reported a value of 255 F/g and Jiang et al used graphene nanomesh and CNTs to report a specific capacitance of 294 F/g.[23,34] Chen et al. used reduced graphene oxide and Ionic liquids to obtain a value of 348 F/g.[61] Wang et all reported a Nitrogen doped graphene mesh based electrode that had a value of 311 F/g.[62] All the references reported a cycling stability above 88%.

3.2.4 Battery Electrodes

Batteries such as the lithium-ion battery are popular energy storage devices that function by storing chemical potential energy and converting it to electrical once placed in a circuit. The structure of a battery consists of an anode, a chemical compound such as a Lithium based salt, a separator and the cathode. The anode is generally a metal coated in a carbon material which allow for permeation and intercalation of ions. The cathode is made of metal oxides with additives to allow for mechanical stability and conductivity. Between the anode

and cathode is the separator, a permeable and nonconductive barrier to prevent direct contact between the anode and cathode as well as to promote Lithium-ion diffusion. Graphene has been considered as a substrate to enhance performance for both anode and cathode materials. Nanoporous graphene can help alleviate a challenge of rapid volume expansion which can occur during the diffusion of Li ions due to insoluble products in the electrolyte. Nanoporous graphene can mitigate the issue by tuning pores that serve as passageways for the insoluble products.[3]

Xiao et al showed a novel Lithium-Air battery using hierarchically porous graphene. Lithium at the anode undergoes a redox reaction donating electrons and generating positive Lithium ions. These ions travel through the porous structure to combine with oxygen in the open air to make $Li_2\ O_2$ and Li_2O. This effectively makes the air on the graphene surface a cathode and shrinks the battery size, weight and cost considerably. However, the reaction products eventually block O_2 pathways and reduce the battery's performance. They noted they would need to optimize pore size for increased performance.[63]

Other nanoporous graphene-based Lithium- oxygen batteries have been constructed by research groups. He et al. used glassy graphene as an electrode for in situ electron microscopic observation of Li- O_2 battery and reported an

initial capacity of 5600 mAh/g .[64] Lin et al. used thermal oxidative etching to form porous graphene cathode to serve as a counter electrode to a lithium anode and reported an initial capacity of 7700 mAh/g.[65]

Lithium-Sulfur batteries have also been explored for the potential application of nanoporous graphene electrodes. Zhao et al used a template growth method to create double layered graphene with perturbations in the two planes which prevents restacking. This structure was then used as a support for a sulfur cathode in a Lithium Sulfur battery and reported 530 mAh/g after 1000 cycles.[66]

3.3 Challenges

Challenges with nanoporous graphene include overall fabrication quality control and scalability. It has proven to be difficult to create large areas of high-quality graphene. A leading approach is the reduction of graphene oxide which generates varied defects. Pores in graphene are not chemically inert to adsorbed carbon atoms which can allow for partial or full recombination. The self-repairing of these defects is likely under excitations which alters the effect of the pores. While the introduction of pores can lead to a desirable increase of surface area, over-introduction of pores will induce a mechanical strength decrease.

Aside from overall challenges such as scalability and pore controllability, each application of nanoporous graphene has individual challenges and prospects.

3.3.1 Separation Challenges

Separation applications require high selectivity to control the separation of mixed gases at the angstrom level. If reliable pore size and high pore density nanoporous graphene layers could be produced, they would make relevant alternatives to current membrane materials. These challenges lie in the fabrication of the layers.

3.3.2 Sensor Challenges

Sensor applications require high surface area and high adsorption rates in order to detect low concentrations of target gasses. Pore size dictates the adsorption properties of the sensors. The desorption process is a challenge as it requires treatment with either heat or UV radiation to remove the adsorbed particles.

3.3.3 Supercapacitor Challenges

Supercapacitors suffer from a comparatively low energy density among energy storage applications. The selection of stable electrodes and electrolytes under high voltages along with increasing surface area through the introduction

of pores helps alleviate the issue. However, to reach full optimization the interaction between electrode pore size and chosen electrolyte must be studied. This also will help avoid pore blockages during charging/discharging cycles.

3.3.4 Battery Challenges

Lithium batteries have been largely implemented into everyday energy storage applications. However, they still are challenged by potential rapid volume expansion during the diffusion of Li ions. Nanoporous graphene can mitigate the issue by tuning pores that serve as passageways for insoluble products. Models can assist in establishing optimal pore dimensions for the kinetic transfer through diffusive channels.

Of these challenges, many stem from adsorption rates on porous graphene. In order to study and optimize these values, molecular dynamics can be used to determine ideal pore size and density for these applications. Literature also calls for a systematic study of adsorption on nanoporous graphene.[3,67]

3.4 Adsorption Overview

Adsorption is the process of free particles being attracted to and settling onto a solid surface. This process differs from the chemical bonding process as it still occurs with atoms of full electron orbitals. The theory starts by

representing the interactions between atoms in an adsorbed layer and the atoms in the surface as a summation of pairwise interactions.

3.4.1 Interatomic Potential

To calculate the interactions between atoms of a given separation one must calculate the total ground state energy of electrons. Considering the interactions between atom A and B with charged nuclei Z_A and Z_B. These atoms will be placed at positions R_A and R_B. The total number of electrons N = $Z_A + Z_B$. The coulombic interactions between nuclei and electrons contribute to the total potential energy as seen in the Hamiltonian:

$$H = \sum_{i=1}^{N} \frac{p_i^2}{2m} - \sum_{i=1}^{N} \left[\frac{e^2 Z_A}{|r_i - R_A|} + \frac{e^2 Z_B}{|r_i - R_B|} \right] + \frac{1}{2} \sum_{i \neq j} \frac{e^2}{|r_i - r_j|} + \frac{e^2 Z_A Z_B}{|R_A - R_B|}$$

The first summation represents the kinetic energy of the electrons, the second summation represents the pairwise coulombic attractive potential energy between the electrons and the atomic nuclei, the third summation represents the coulombic repulsion between electron pairs and the final term gives the potential energy contribution from the atomic nuclei. The Hamiltonian is a function of atomic separation $R = |R_A - R_B|$.

From quantum mechanics and Dirac's formalism, the ground state energy is the lowest energy solution to the eigenvalue equation:

$$E(R) = \langle \Psi | H | \Psi \rangle$$

With Ψ is the total wave function for N electrons. At large interatomic distances the total energy will consist only of two atoms in their ground state, $E_0^A + E_0^B$. Therefore, the interatomic potential, $V(R)$, contributes to the total energy in the following fashion:

$$E(R) = V(R) + E_0^A + E_0^B$$

Or

$$V(R) = E(R) - E_0^A - E_0^B$$

At large separations of $R = \infty$, $E(R) = E_0^A + E_0^B$ so $V(R)$ approaches zero at large distances. On the other hand, at small separations of $R = 0$, both $E(R)$ and $V(R)$ approach infinity. Between these extremes is a potential well that is determined by the particular species of atoms.

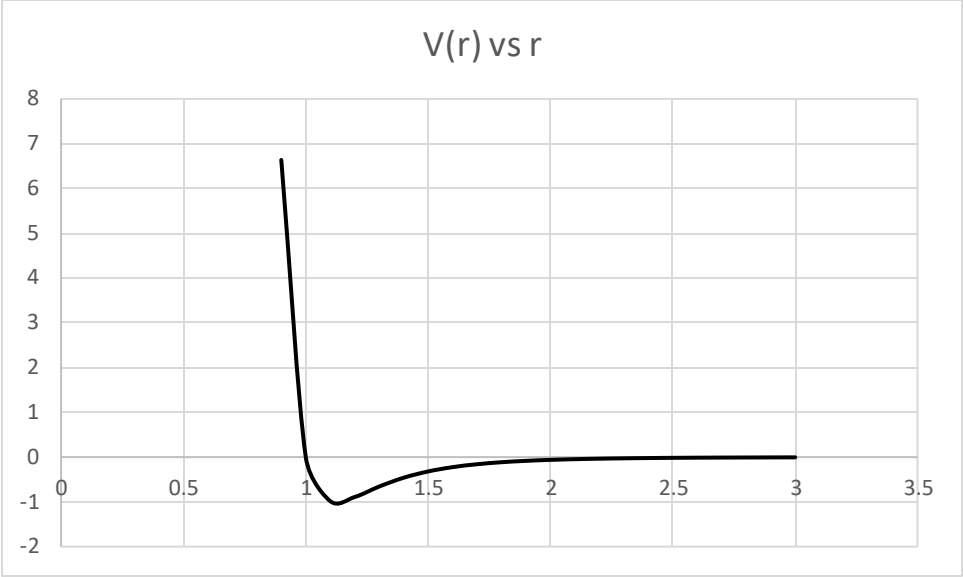

Figure 8 Derived interatomic potential, V, plotted against separation distance, r

This function's shape has been well researched and is well modeled by the Lennard- Jones or 12-6 potential. As it pertains to adsorption, atoms in the surface can be understood as one of many atomic nuclei A, while the adsorbate can be understood as one of many atomic species B. Each atom in the adsorbate receives a potential energy contribution from each atom in the surface, the summation of which determines the total potential energy. Furthermore, the negative gradient of the potential energy gives the force on the adsorbate particle. Historically, this force had been observed and was dubbed the Van Der Waal's Force.

The Van Der Waal's force describes an interatomic potential that explained the process of adsorption prior to quantum theory. The notable properties of the Van der Waal's force were that it was relatively weak when compared with ionic and covalent bonds, they are short range interactions, and they can be attractive as well as repulsive. Eventually, this force was shown to be due to a group of other mechanisms. The close-range repulsion comes from the Pauli exclusion principle, while the intermediate behavior is partially due to instantaneously induced dipoles and quadrupoles and the electrostatic forces between them. In the case of an interaction between an induced dipole with a permanent one the force was dubbed the Debeye force. In the case of interactions between multiple induced dipoles, the force was referred to as the London Dispersion Force. In closed shell, charge neutral cases, the culmination of these forces can be modeled with the Lennard Jones Potential.

3.4.2 Lennard-Jones Potential

The Lennard-Jones potential has the following form:

$$U(r) = 4\varepsilon(\left(\frac{\sigma}{r}\right)^{12} - (\frac{\sigma}{r})^{6})$$

U is potential energy as a function of r, separation distance. ε is the well depth scalar at its deepest which occurs at $r = 2^{1/6}\sigma$,and σ is the distance where U crosses 0 on the repulsive side called the Van der Waal radius. The

potential is graphed above. Both σ and ε are specific to the atom that is producing the potential. These values are obtainable in literature.[68]

The $\left(\frac{1}{r}\right)^{12}$ term is representative of the Pauli repulsion at short distances and the $(\frac{1}{r})^{6}$ term is consistent with the london dispersion force. At short ranges the Pauli repulsion is dominant, sending the potential to infinity. At large ranges, both terms vanish bringing the potential to zero. At intermediate ranges the London dispersion forces are enough to create a potential well. Computational programs employ the Lennard-Jones potential to calculate the potential contributions across huge numbers of particles. Allowing programs to simulate the evolution of systems with the use of the Lennard-Jones potential also allows for the calculation of quantities of interest in adsorption.

3.4.3 Adsorption Quantities

The quantities of interest in adsorption are Specific Surface Area and Adsorption Capacity. These values describe the adsorption surface in terms of site availability and amount. Specific surface area is defined as the surface area (SA) per unit mass. This value is measured in $m^2 g^{-1}$.

$$SSA \stackrel{\text{def}}{=} \frac{SA}{m}$$

Adsorption Capacity is defined as the mass of adsorbate on a sample's surface per unit mass of the sample. This value is primarily measured in milligrams per gram.

$$Adsorption\ Capacity \overset{\text{def}}{=} \frac{m_{adsorbate}}{m_{adsorbent}}$$

These quantities are how researchers evaluate and compare the adsorption ability of various structures. As mentioned earlier, one structure of interest for adsorption focused applications is Nanoporous Graphene

3.5 Theoretical Experimental Specific Surface Area Discrepancy

High specific surface area plays a significant role in nanoporous graphene adsorption. Yet, it is not fully understood. There is a discrepancy between experimental and theoretical values for graphene specific surface area. This section will introduce the discrepancy.

Specific surface area is an important factor in determining graphene's adsorption applicability. However, there have been discrepancies between theoretical and experimental determination of graphene's specific surface area.

3.5.1 Theoretical Determination

Theoretical calculations reveal that the maximum specific surface area is of graphene is $2630\ m^2/g$. This is calculated by recognizing that carbon atoms in graphene form a hexagonal lattice. The area of a regular hexagon is $A = \frac{3\sqrt{3}}{2}s^2$, where s is the length of a side. The carbon-carbon bond length in this case is equal to .142 nm. The hexagonal area is calculated to be .05238 nm^2 or $5.23 * 10^{-20} m^2$ As the sheet has two sides, this surface area should be doubled.

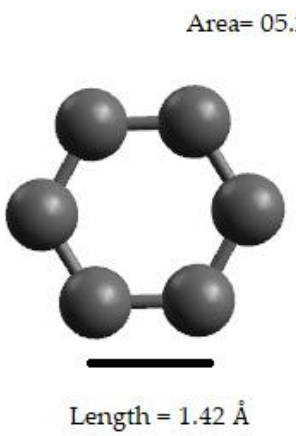

Figure 9 Dimensions and Area of Carbon Hexagon

Each carbon atom is shared between 3 hexagons, so to avoid counting the same carbon atom repeatedly only 1/3 of its mass needs to be accounted for. 1 hexagon has 6 carbons with 1/3 of the mass needing to be calculated. Carbon has

a mass of 12.911 amu. The average mass in a hexagon is $6\left(\frac{1}{3}\right)(12.011)$amu = 24.022 amu or $3.99 * 10^{-26}\ kg$. Specific surface area is defined as Surface Area divided by Mass.

$$SSA = \frac{SA}{m} = \frac{10.46 * 10^{-20} m^2}{3.99 * 10^{-26} kg} = 2621.6 \frac{m^2}{g}$$

Experimental results disagree with this value in a suspicious fashion. As this value is already quite large, one would expect experimental values to be less. However, experimental values have been higher than the theoretical value. This is alarming due to the theoretical calculation being calculated as a maximum value.

3.4.3 Experimental Determination

The experimental determination of specific surface area depends on adsorption of a known ideal gas such as Argon or Krypton. From the ideal gas law, the product of pressure, P, and volume, V, is equal to the product of particle number, N, Boltzmann's constant, K and temperature, T. PV=NKT. Experiments place a surface in a chamber of known volume. They hold temperature constant while monitoring pressure as the gas gets adsorbed onto the sample. The difference between starting and ending pressure after adsorption reaches a saturation point allows for the determination of particles adsorbed on a samples

surface. These values give the effective surface area by multiplying the monolayer amount n_m, the average area per gas particle, a_m.

$$SA = n_m * a_m$$

Division by the sample's mass allows for the determination of a sample's specific surface area. Some reported values following this methodology are higher than the theoretical value for specific surface area. Herein lies the discrepancy between experimental and theoretical specific surface area of graphene.

3.4.3.1 BET Experimental Determination

The Brunauer, Emmet, Teller (BET) theory allows for the calculation of Specific surface area (SSA) from a isotherm of types II and IV. The BET approach for deriving specific surface area involves creating a BET diagram from isothermal data. The BET equation is the following:

$$\frac{\frac{p}{p_0}}{\left[n_a\left(1-\frac{p}{p_0}\right)\right]} = \frac{C-1}{n_m C}\frac{p}{p_0} + \frac{1}{n_m C}$$

In this equation p is pressure, p_0 is pressure of saturation, n_a is adsorbed molecule number, C is the BET parameter which is related to enthalpy of surface adsorption and vaporization. n_m is the monolayer amount.

When this equation is evaluated at relative pressure, $x = \frac{p}{p_0}$, values between .05 and .3 one can plot a linear relationship. To accomplish this, BET plots let :

$$y = \frac{\frac{p}{p_0}}{\left[n_a\left(1 - \frac{p}{p_0}\right)\right]}$$

A BET plot gives a straight line where the slope is called a and the y-intercept is called b. Slope is calculated from change in y divided by change in x and the y- intercept is derived from linear regression. From these 2 values one can solve for the monolayer amount $n_m = 1/(a + b)$

After one knows the monolayer amount, one can find the average area occupied by an adsorbed molecule, a_m in literature. From these values one can find the effective surface area by multiplying the monolayer amount, the avg area per molecule and the number of layers, L.

$$SA = n_m * a_m * L$$

CHAPTER 4

THESIS AND PRELIMINARY RESULTS

4.1 Proposed Discrepancy Resolution

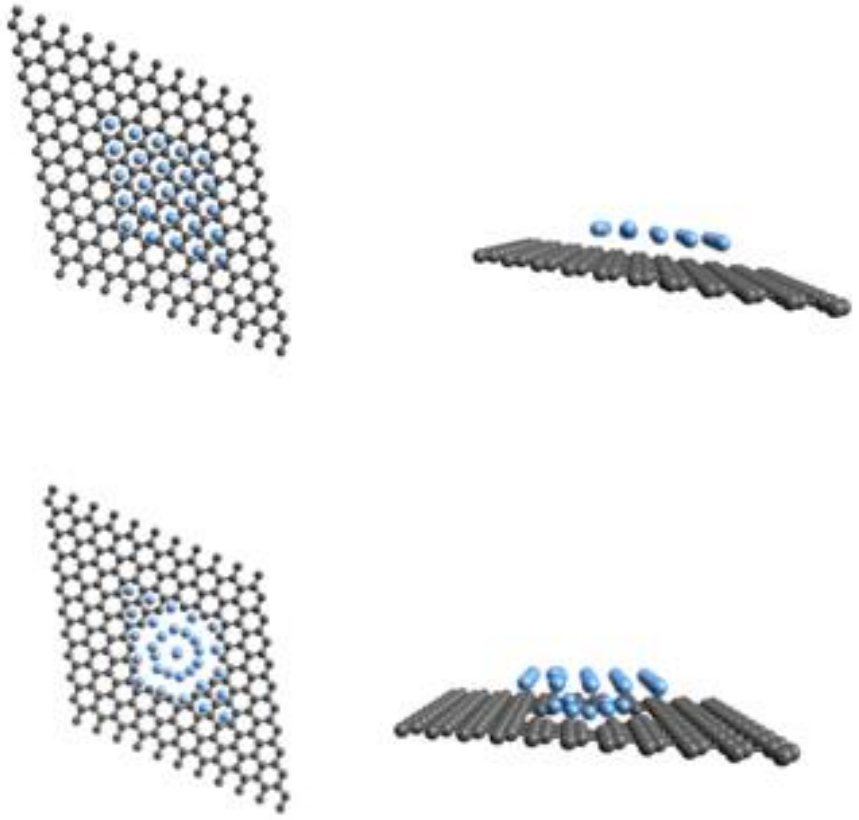

Figure 10 Adsorption Sites on ideal graphene (above) vs defective graphene (below)

The proposed explaination for the experimental-theoretical discrepancy is the presence of defects on the experimental graphene surface. Vacancy defects

act as adsorption sites that allow for a larger number of particles to attach to the surface of the sample, giving it a higher effective surface area than an ideal sample.

A correlation between pore volume and specific surface area of porous graphene has been documented. However, this is not true for pores of all sizes. Potential defects in graphene surfaces can lead to experimental values greater than theoretical values for specific surface area in what is thought to be ideal graphene. Regardless, the effect of porosity on adsorption must be systematically studied.

4.2 Preliminary Justification Experiment

Previous work has been done to justify this thesis. A potential energy line has been calculated for ideal graphene, and pore diameter sizes of 5.7 Å, 7.54 Å and 10.28 Å. Data points with potential energy values too large for the graph are removed in the figure.

4.2.1 Justification Experimental Results

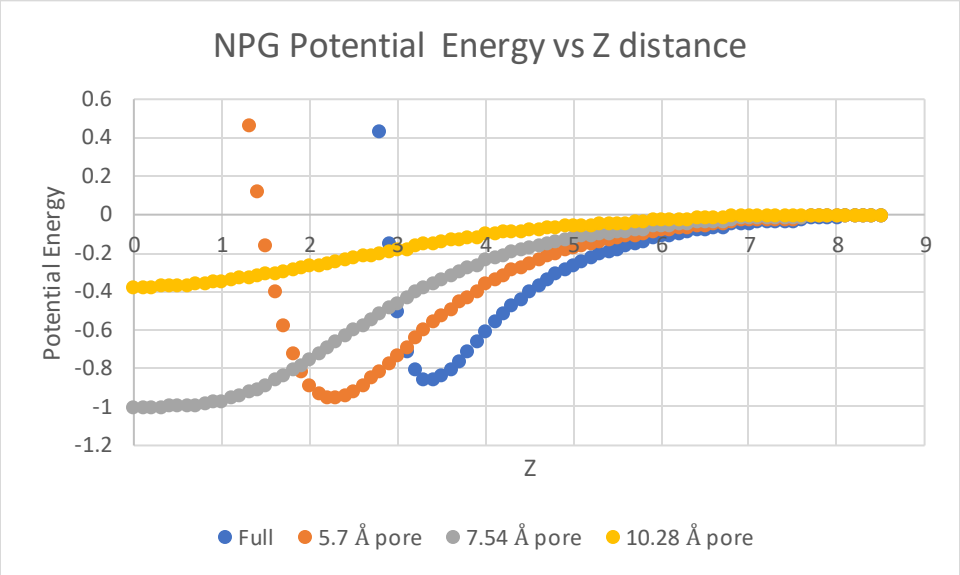

Figure 11 Potential energy vs distance along z axis for ideal graphene and nanopore diameters 5.7 Å, 7.54 Å and 10.28 Å

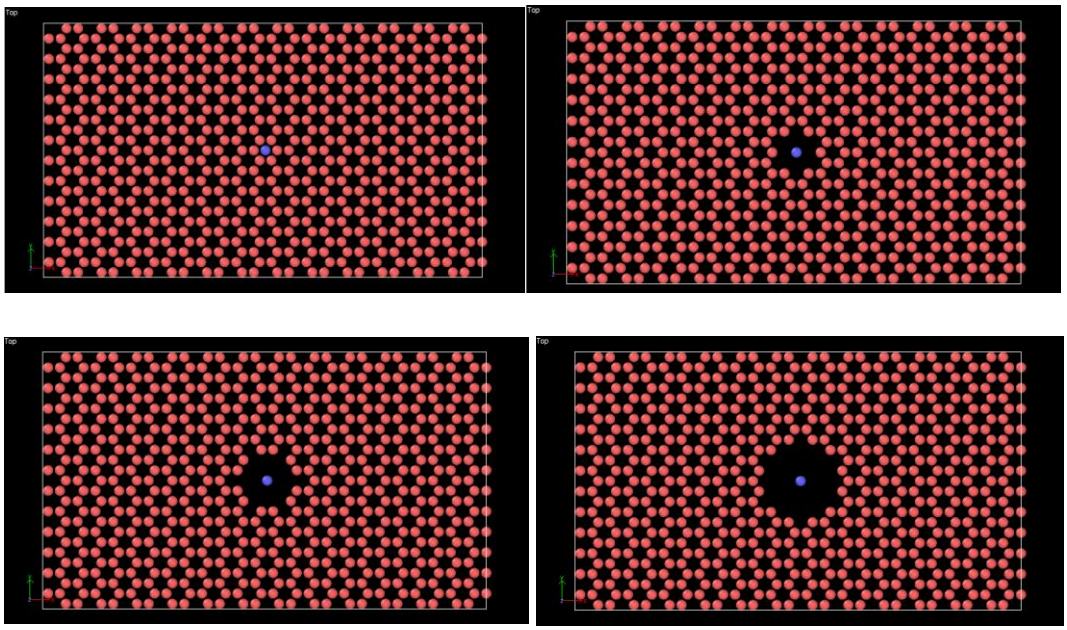

Figure 12 Top view of ideal graphene, and nanopore diameters of 5.7 Å, 7.54 Å and 10.28 Å

This figure shows that introducing pores creates a deeper, wider potential well up to the case of 7.54 Å diameter pore. At 10.28 Å diameter pore, the potential well becomes shallow. Analysis of this gives confidence that porous graphene does indeed increase adsorption rates over ideal graphene as expected from literature. This increase is due to the removal of the nearside repulsion in the lennard jones potential in the porous region. Also this is in line with what one expects to see from pore sizes that get too large.

4.2.2 Preliminary BET Isotherm Results

A preliminary adsorption isotherm was created with molecular dynamics in order to demonstrate the capability. This script created a 298 Kelvin isothermal compression from 5 atm to .5 atm. The exported data recorded the amount of Ar atoms within a region above the graphene surface as the pressure increased. From this data Surface Area the calculated value is 1950.82 m^2/g. This is 25% lower than the theoretical value of 2630 m^2/g. The calculated adsorption capacity of Ar on ideal graphene was 107.65 mg/g. For comparison rGO reportedly had an carbon dioxide adsorption capacity of 147.4 mg/g.[69]

CHAPTER 5

ANALYTICAL DISCUSSION

5.1 Geometrical Approach

The theoretical determination of graphene's specific surface area employs a geometrical approach. Extending this approach to graphene with vacancy defects can give an approximate value to specific surface area changes due to pore introduction.

A single vacancy defect will induce a pore the size of three hexagonal areas. However, the walls of the pore will now provide a contribution to the surface area. The difference between the lost hexagonal areas and the gained pore walls will determine the change in surface area from ideal graphene. The area of a regular hexagon is $A = \frac{3\sqrt{3}}{2}s^2$, where s is the length of a side, in this case .142 nm. The pore wall will be approximated as a summation of rectangles with the length being the bond length, .142 nm, and the width being the atomic thickness, .34 nm. The number of rectangles will be the amount of exposed bonds surrounding the perimeter of the pore.

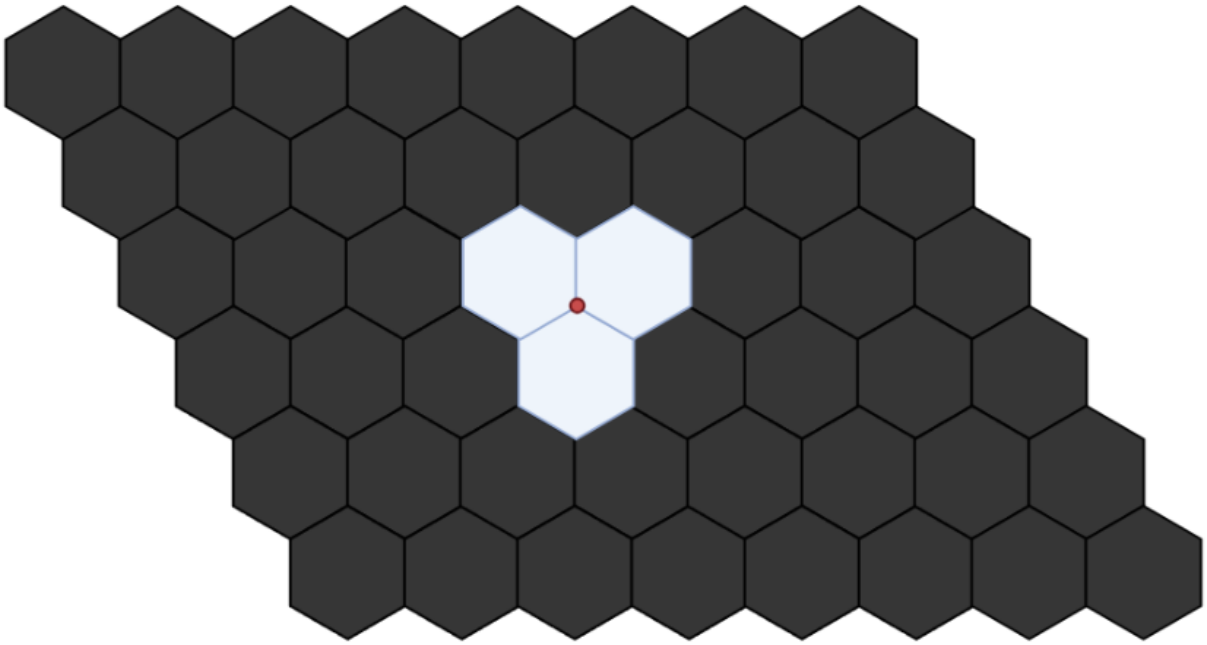

Figure 13 Geometrical Structure of Graphene with a single vacancy defect. This case is labelled as an “atom centered” pore

In the case of a single vacancy defect three hexagonal areas are broken. In doing so the perimeter of the introduced pore is exposed to the environment. There are 12 bond lengths revealed in this case. The hexagonal area, A, loss is doubled due to there being a top and bottom surface contribution to surface area. The 12 bond lengths, s, are multiplied by the pore depth, d, to find the contribution to the total surface area. This means the surface area difference is the following.

$$\Delta SA = \ 2(3A) - 12(s)(d) = -2\left(3\left(\frac{3\sqrt{3}}{2}(.142)^2\right)\right) + 12(.142)(.34)$$

$$= \ .265nm^2$$

This shows that the introduction of a single vacancy defect very slightly increases the surface area from a geometrical standpoint. It should be mentioned that with regards to specific surface area the removal of a carbon mass the denominator would decrease as well making the specific surface area increase more.

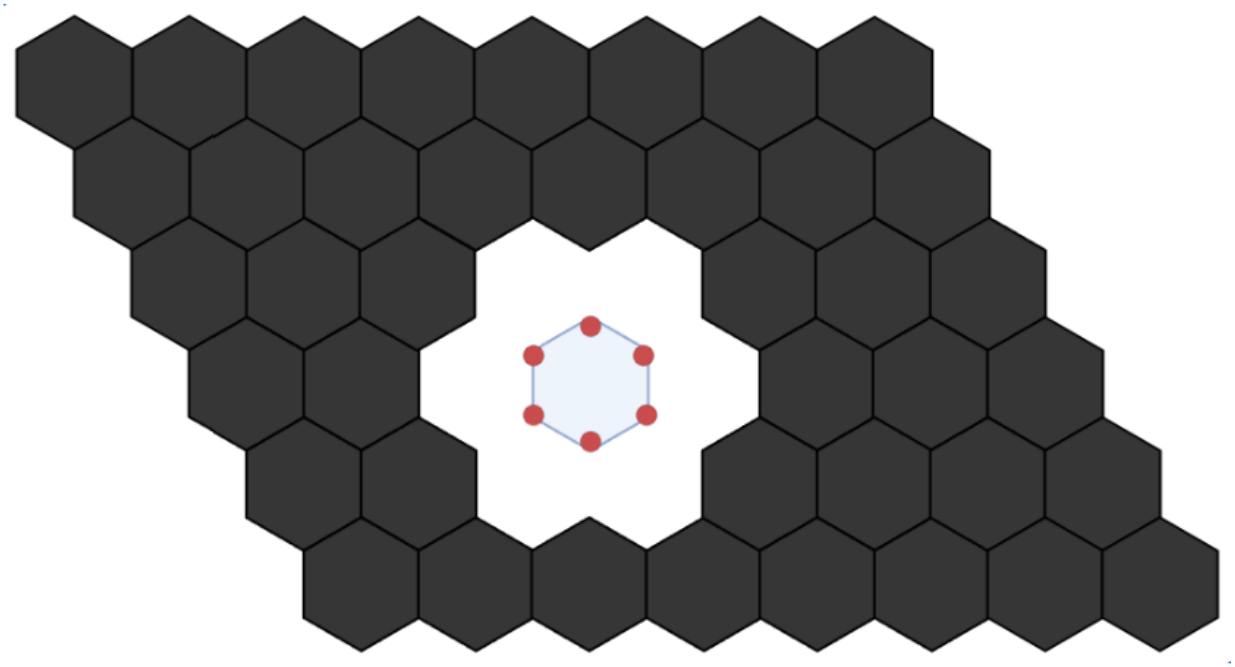

Figure 14 Geometrical Structure of Graphene with 6 vacancy defects in the shape of a hexagon. This case is labelled as a "ring centered" pore

In an effort to include varied pore geometries, a ring of carbon atom vacancies will be considered. This case removes 7 hexagonal areas and gains 18 pore perimeter walls. Following the same calculation as above the increase in surface area for this case is $.136nm^2$. A larger pore size gave a lower increase than the singular vacancy case, albeit with altered pore geometry.

Increasing the amount of vacancy defects with both pore geometries leads to a decrease in surface area. Specifically, the initial pore geometry, centered on the single carbon vacancy, 13 vacancies led to a decrease in surface area of $.099nm^2$. For the ring centered pore geometry, 24 vacancies led to a decrease in surface area of $.54\ nm^2$. A table of pore geometry, vacancy count and surface area change is below.

Table 1. -- Surface area changes from Ideal graphene base on pore geometry, vacancy counts

Pore Geometry	Vacancy Count	Surface Area Change (nm^2)
Atom centered	1	0.265034348
Atom centered	4	0.240388695
Atom centered	13	-0.098582609
Ring centered	6	0.135613478
Ring centered	12	0.086322173
Ring centered	24	-0.542329132

5.2 Pore Volume Analysis

In the experimental approach, counts of adsorbed atoms are multiplied by the cross-sectional area of the adatoms in order to determine a specific surface area. The belief is that atoms inside the pores generated by vacancy defects are being counted among the adsorbed atoms leading to an over-estimate of specific surface area. However, a pore volume of given dimension would be able to contain a limited number of adatoms meaning there should exist a limit to the potential overestimate based on pore volume. Below is a table of the possible

contribution to specific surface area based on adatoms found in pores of previously discussed dimension.

Table 2.--Surface Area contributions due to the maximum amount of Argon adatoms adsorbed in pore volume.

Pore Geometry	Vacancy Count	Pore Volume (nm^3)	Ar in Pore	SA Contribution (nm^2)
Atom centered	1	0.0534	35	0.5542705
Atom centered	4	0. 106871	71	1.124377
Atom centered	13	0. 213741	142	2.248755
Ring centered	6	0.124682	83	1.314413
Ring centered	12	0.231553	154	2.438790
Ring centered	24	0.338423	225	3.563167

While these values are all positive, they are all nearly negligible when compared with the Ar counts of the entire surface, on the order of 20,000. This leads to the belief that the increase in specific surface area is not only due to atoms within the pores, but also the atoms in the volume near to the pores.

5.3 Extended Pore Volume Expectation

The analytical discussion gives relevant information about the amount of surface area contributed from the introduction of vacancy defects in a graphene lattice. From these arguments alone, it would not be reasonable to expect that a vacancy defect would increase Graphene's specific surface area by values on the order of 100 $m^2 g^{-1}$. For this reason, the distinction should be made between a surface area increase and an effective surface area increase.

The distinction is thus, when one is determining the specific surface area of a sample, the main contributing number is the number of adatoms that are accounted as adsorbed. This number may be higher for some samples based on their attractive nature. In the case where more than a simple monolayer forms across the surface, excess atoms are counted among those adsorbed. The physical surface area does not increase, but due to the increase in adatoms, the effective surface area will increase.

Nevertheless, a high effective surface area is just as attractive for adsorption applications. The analytical discussion of pore volume assists in localizing the adatoms that are contributing to the effective surface area increase. From this information, it is expected that the main increase in specific surface area is not specifically due to adatoms within pores, but likely also in the nearby volume.

CHAPTER 6

OVERVIEW OF MOLECULAR DYNAMICS EXPERIMENT

6.1 LAMMPS and OVITO

Large-scale Atomic/Molecular Massively Parallel Simulator or Lammps is a powerful molecular dynamics program with open availability and the capability of materials modelling. Lammps operates by following an input script which details the specifics of a simulation. The input script lists commands that a user details from a huge selection of possibilities. Due to the large availability of commands, lammps is a widely-used and powerful tool for simulation at the atomic, meso and continuum scales. [70] LAMMPS is well suited for this work due to it's large-scale capabilities. Work will need to account for multiple scale ranges from, with an amount of particles that will exceed ab initio calculation abilities.

A project begins by connecting to a computational computer. The computer has the molecular dynamics simulation program, Large-scale Atomic/Molecular Massively Parallel Simulator or LAMMPS, able to run. The command lmp -in "inputfilename" instructs the program to run a simulation based on the parameters set by the input file. The input file is a script that instructs the program to perform a series of commands.

6.1.1 Scripting

The script is generally broken up into four main portions. The first, initialization, defines the basics of the system. Defined here are the units, dimensions, boundary conditions, atom style, bond style and simulation volume. Command keywords, such as “real” units, are further defined in the Lammps manual.

The second portion of the script pertains to atom and force definition. The commands define positions and interatomic potentials for atoms either manually or by reading from another data file. Following this is a settings and equilibration step in the input script.

The third section of the script prepares the system for the simulation. This portion of the script contains settings for the simulation timestep and applies fixes to the system to bring it to a desirable initial state.

The fourth and final section of the script is the deformation portion where the desired effects of the simulation take play in the form of fixes. The dump command exports the requested data every given number of steps. The thermo section allows us to track the ongoings of the simulation until it is complete. The exported files are then viewed in OVITO (open visualization tool) to gauge if the simulation ran appropriately.

The exported files can be modified within OVITO. Under the add modification section of the program one can use the delete selected atoms modification. Then all the selected atoms will be removed from the display and any future export files. This allows for the introduction of pores of any desired size and location. The modified sheet is exported into a Lammps data file and can be placed into an identical script for comparison. This altered script exports its own set of dump files and a log file.

LAMMPS and the input script are important for this work because of its division of sections. Altering one of the sections while keeping the others the same allow for quick, simple repeatability. This assists in the comparison of similar simulations. Specifically, the initial structure of the porous graphene layers will be altered, then the potential energy calculations and isothermal compression will remain the same across trials. This allows for simple debugging procedures as it will immediately determine the location of an error if a simulation fails.

6.1.2 OVITO

Open VIsualization Tool (OVITO) is an open software that is useful for viewing and manipulating files produced from various molecular dynamics packages. LAMMPS dump files are one of the file types that OVITO is equipped

to view manipulate. OVITO is used to introduce pores into graphene layers and export data files that can subsequently be placed into LAMMPS simulations.

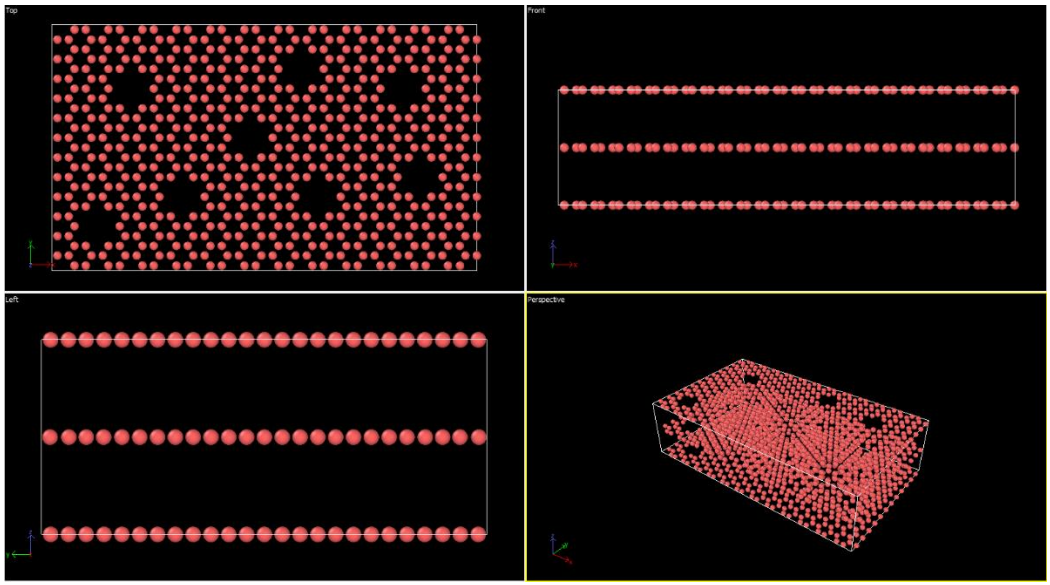

Figure 15 Example of OVITO visualization and system manipulation

6.2 Experimental Goals

The goal of the experiment is to obtain adsorption data of Argon in the porous region of nanoporous graphene and resolve the theoretical- experimental specific surface area discrepancy. The experiment is constructed to provide adsorption counts in a volume around the surface of ideal graphene as well as porous graphene of increasing pore diameters. The data provided will show if extra available adsorption sites are in the pores and the extent to which pore size and density factor into additional adsorption. Defects in pristine graphene will

lead to an increase in adsorption capacity and specific surface area due to a porous contribution.

6.2.1 Experimental Scope

The scope of this experiment falls in line with the capabilities of LAMMPS, which is a largely classical mechanics-based software. For a first principles calculation, ab initio simulation programs may be considered. However, ab initio approaches historically struggle with systems of high particle numbers, such as this work. Furthermore, LAMMPS is sufficient for this system as it consists of closed shell, monatomic particles such as Argon, where the Lennard-Jones potential models the system very closely.

6.3 Design and Data Acquisition

To achieve this goal and gather the necessary data, a molecular dynamics program will be used. The program will create a 3-dimensional simulation volume with periodic boundary conditions. A hexagonal lattice will be formed in the volume. The crystal parameters for graphene are a = 2.47 A, b =2.47A, c = 7.80 A and α= 90 degrees β = 90 degrees γ = 120 degrees. Basis vectors are taken as (0, 0, 0) and (1.234, 0.712 ,0). Carbons are placed at these lattice sites to generate ideal graphene along the x-y plane. Argon atoms are then generated in the simulation box at random locations that don't overlap the graphene layer.

The chosen interatomic potential is a Lennard Jones potential with a cutoff distance. Interatomic parameters and atomic masses are found in literature. A region of interest is defined around the graphene layer. Since the carbon hard shell radius and cutoff distance are known, the adsorbed region will be defined as the z-values between these distances on both sides of the graphene layer. This region is where an adsorbate monolayer will be formed.

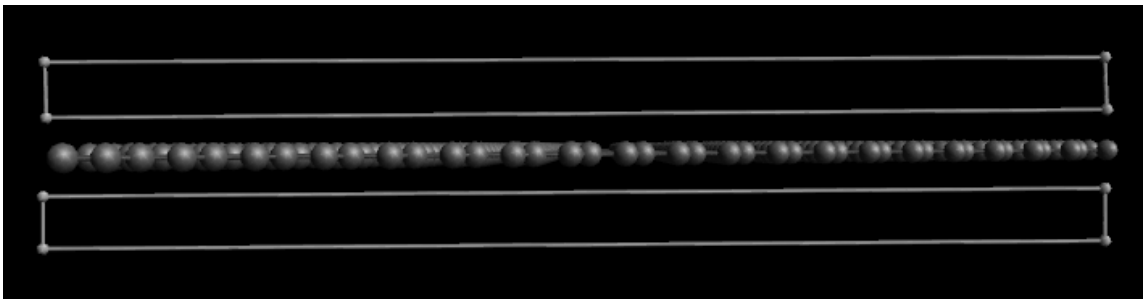

Figure 16 Representation of adsorption defined region on ideal graphene.

Prior to any deformation, potential energy calculations will be made for z values above the graphene layer. This will give information on the adsorptive forces in more complicated porosities. This data will be analyzed for the strongest attraction across the pore structures.

The project then calls for an energy minimization command in order to get the atoms into a realistic starting position. The next step is to apply a fix to the system that brings the temperature of the system to a desired starting point. The thermo output section enables for the program to display the ongoings of the

simulation on a terminal screen. Useful values to monitor include the step, pressure and temperature of the system.

This simulation will call for a fix to run an increase the pressure, the units of which were previously defined as atmospheres. As the compression runs, a compute is made to track the amount of atoms in the adsorbed region as well as a specified porous region. This data will give values for the count of atoms in each pore. Analysis of this can give a value for specific surface area overestimation based on pore sizes.

Adsorption Capacity is a measure of a substance's ability to attract and retain particles through interatomic attraction. In gasses it is defined as the amount of adsorbate taken up per unit mass of an adsorbent with the units of mg/g. These values will also be obtained through the experiment.

The project exports the requested data every given number of steps. Again, the thermo section allows the ability to track the ongoings of the simulation until it is complete. The exported files are then viewed in OVITO (open visualization tool) to gauge if the simulation ran appropriately.

OVITO also allows for the introduction of pores into the graphene layer. After the desired porosity is introduced, the structure will be read into the simulation and the procedure will be repeated.

6.4 Data Management

Dump files and Log files are exported from the computational computer to a local system. Data is managed using Microsoft Excel. Input files are saved on the computation computer in case there is a need to recreate a simulation.

6.5 Results

6.5.1 Pore Geometry

The two types of pore geometries evaluated in this work are defined as atom centered and ring centered pores. Atom centered pores are the case where a single carbon atom is removed and subsequently grown from there. Ring centered pores are grown from a ring of vacancy defects instead.

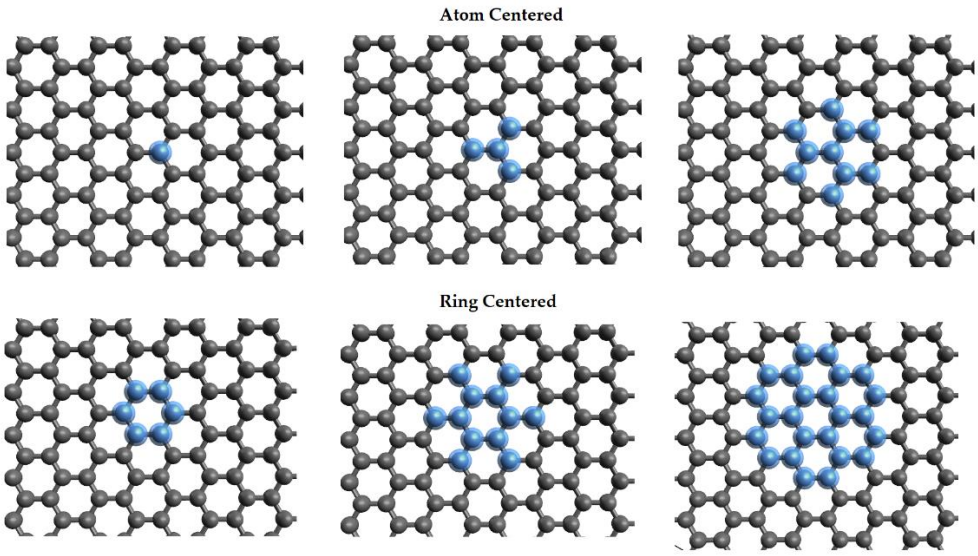

Figure 17 Vacancy Defect Sites for Pore Geometries

6.5.2 Potential Energy vs Z distance

Potential Energy was calculated along an axis perpendicular to the graphene surface. A group of pores have been generated centered on either a carbon atom or centered on the central gap in a carbon ring. Potential energy at each site is calculated by summing the lennard-jones potential energy contributions from all atoms within the cutoff distance.

6.5.2.1 Potential Energy for Ring Centered Pores

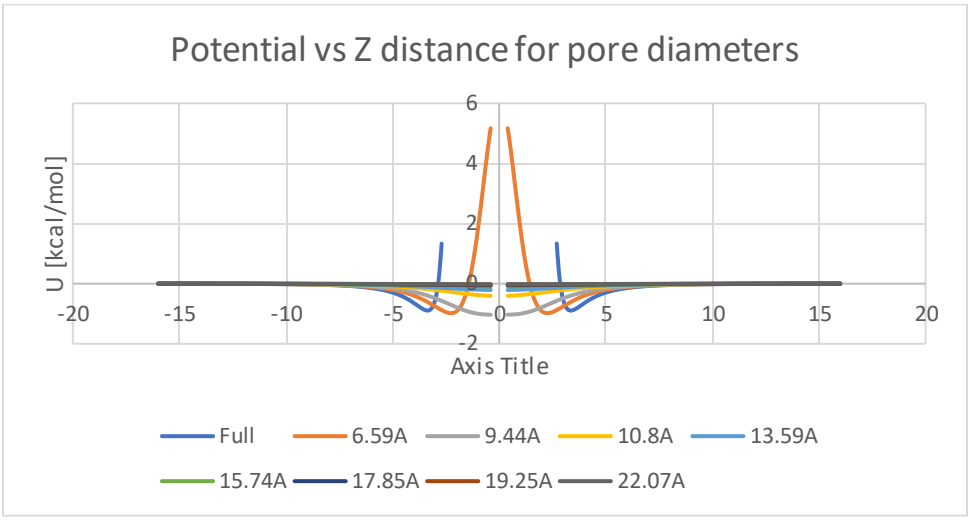

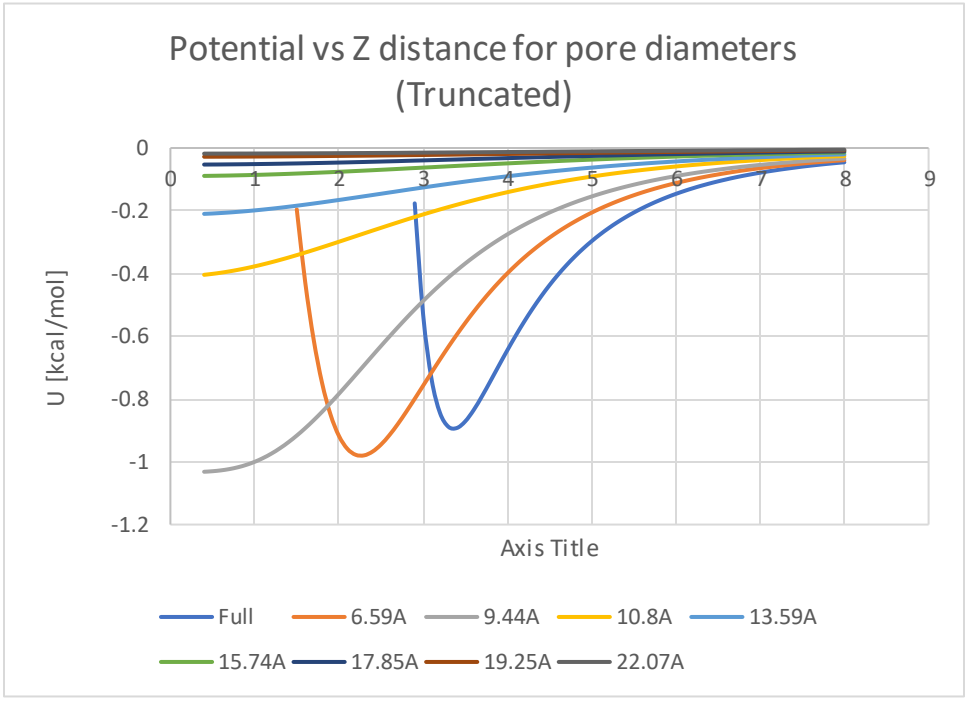

Figure 18 Potential along Z axis for varied pore diameters

Shown in figure 16 are the potential energy results calculated from z=-16 to z=16. Pore diameters include zero, 6.59, 9.44, 10.8 13.59, 15.74, 17.85, 19.25 and

22.07 Angstroms. The lower figure shows the same results with z values above 0 and potential energy values above 0 removed.

This graph shows that as pore size increases, the potential energy well initially becomes deeper, and the nearside repulsion is effectively removed at pore diameters of 9.44 Angstroms. Pore diameters larger than this create increasingly shallow potential energy wells becoming near zero at 17.84 Angstroms.

6.5.2.2 Potential Energy for Atom Centered Pores

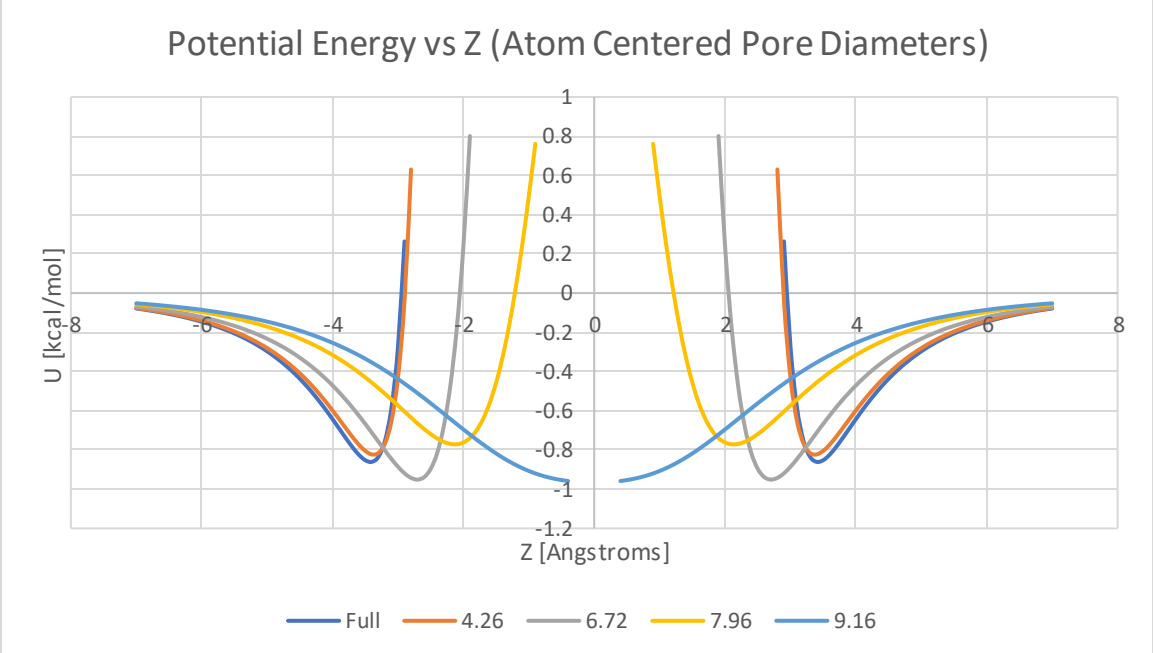

Figure 19 Potential Energy vs z distance for Atom centered pores

This figure shows the changes in potential energy wells for pores generated from the atom centered cases.

6.5.3 Potential Energy vs Radius

Potential energy calculations were performed along the pore diameter in the graphene plane. As expected, there is a potential well inside the pores. This information is useful when comparing the differences between pore geometries.

6.5.4 Specific Surface Area

Specific Surface Area was calculated through the adsorption method for both configurations of pores, ring centered, and carbon centered. specific surface area calculated directly from dimensions of the simulation volume is calculated to be 2627.164 m^2/g

6.5.4.1 Specific Surface Area for Ring Centered Pores

Table 3. -- Effective Specific Surface Area for Ring Centered Pores

Pore Diameter (Å)	Carbon Count	Effective Ar Count	Effective Specific Surface Area ($m^2 g^{-1}$)
Ideal	62500	18922	2504.625
6.59	62494	21621	2862.155
9.44	62488	21600	2859.65
10.8	62476	21596	2859.669
13.59	62464	21570	2856.775
15.74	62446	21541	2853.757
17.85	62428	21517	2851.399
19.25	62404	21499	2850.11
22.07	62380	21455	2845.371
22.7	62350	21450	2846.076
24.18	62320	21416	2842.933
29.2	62284	21314	2831.028

6.5.4.2 Specific Surface Area for Carbon Centered Pores

Presented below are the effective specific surface area for various pore sizes for the atom centered pore case.

Table 4. -- Effective Specific Surface Area for Atom Centered Pores

Pore Diameter (Å)	Carbon Count	Effective Ar Count	Effective Specific Surface Area $(m^2 g^{-1})$
Ideal	62500	18903	2502.11
4.26	62499	22189	2937.111
6.72	62496	22176	2935.531
7.96	62490	22173	2935.416
9.16	62487	22164	2934.365
14.3	62463	22084	2924.897

6.5.5 Adsorption Capacity

6.5.5.1 Adsorption Capacity for Ring Centered Pores

Table 5 contains Ring centered pore Adsorption Capacity values.

Table 5. --Adsorption Capacity for Ring Centered Pores

Pore Diameter (Å)	Adsorption Capacity (mg/g)
Ideal	1006.938
6.59	1150.677
9.44	1149.669
10.8	1149.677
13.59	1148.514
15.74	1147.3
17.85	1146.352
19.25	1145.834
22.07	1143.929
22.7	1144.213
24.18	1142.949
29.2	1138.163

6.5.5.2 Adsorption Capacity for Carbon Centered Pores

Presented in table 6 are the adsorption capacity for various pore sizes for the atom centered pore case.

Table 6. -- Adsorption Capacity for Carbon Centered Pores

Pore Diameter (Å)	Adsorption Capacity (mg/g)
Ideal	1005.927291
4.26	1180.811394
6.72	1180.176235
7.96	1180.129879
9.16	1179.7075
14.3	1175.901037

6.6 Analysis

6.6.1 Porous Contributions

It is shown that all the pore values for both geometries have higher adsorption capacity and effective specific surface area over the ideal graphene case. It is indeed possible that the specific surface area discrepancy is due to vacancy defects in experimental samples.

6.6.2 Pore Geometry Effects

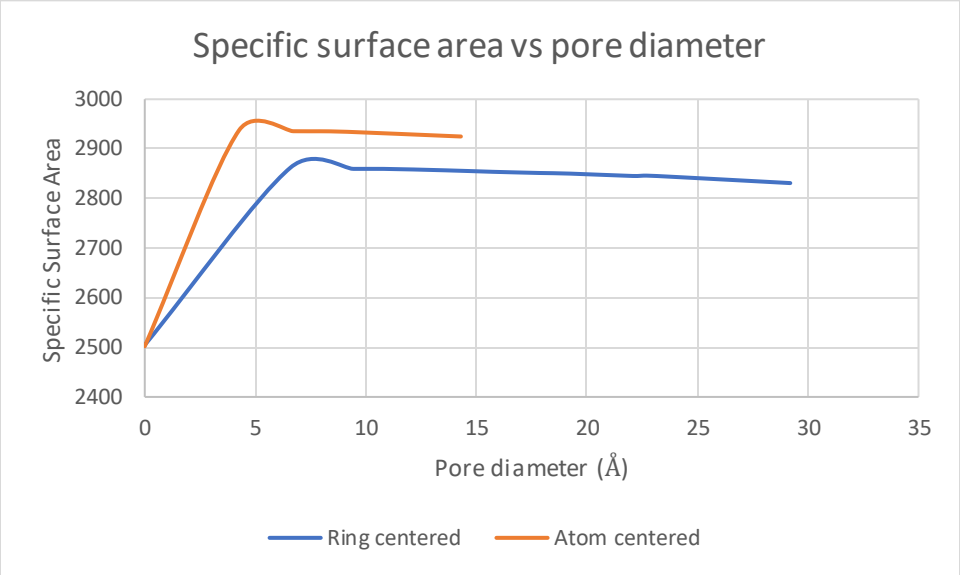

Figure 20: Pore Geometry effect on specific surface area

Ideal graphene's specific surface area calculated from adsorbed Argon counts is below the theoretical value by ~100 m^2/g. The largest specific surface area increase for both gap centered and carbon centered pores are from ideal to the smallest pore size. Increasing the pore size also increases the specific surface area but by comparatively small amounts. Therefore, the largest impact on graphene specific surface area from pores come from the introduction of a pore, small or large. The main contributor to the increase in adsorbed Argon is outside of the porous cylinder. This indicates that significantly more adsorption sites appear especially outside the porous cylinder as a pore gets introduced.

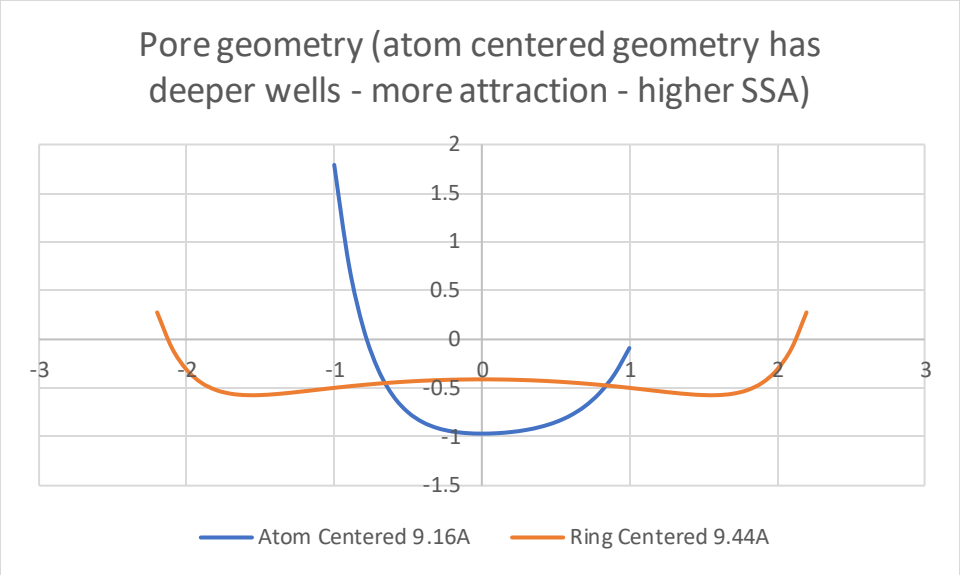

Figure 21 Atom centered pores with deeper wells than Ring centered pores

Carbon centered pores produce larger specific surface area than gap centered pores due to the structural differences. Z-value positions for the Carbon centered cases will be closer to nearby carbon atoms. These values will closer to the lowest parts of the potential produced by nearby carbon atoms when compared with the gap centered cases.

This helps to show that in the case of a vacancy defective graphene surface, no matter how small the vacancy, the specific surface area will be notably increased. It then stands to reason that experimental determinations of ideal graphene's specific surface area higher than the theoretical value can be explained by the presence of vacancy defects.

This shows that vacancy defects in graphene increase both the Specific Surface Area and the Adsorption Capacity of the structure.

5.6.3 Localizing Largest Contributions

A follow-up simulation was created to localize the highest Argon count in volumes around the pore. A cone shaped region was formed to find the contribution to Argon adsorption increase. This cone was placed over with the vertex 5.76 Å over the single atom centered pore. It was found that a cone with a 134 Å radius held a 73.4% contribution to the increase in Ar atom counts. Most of the specific surface area increase occurs in this conical volume, which is 11.4% of the adsorbed region's volume.

An explanation for why the Argon increases in this region is due to the effects of a lowered Argon atom in the introduced pore. As one atom sinks into the pore, nearby atoms can cover it, leading to an overlap in atoms that contribute to effective surface area. This overlap creates a ring of added effective area increase that grows with the distance from the pore. This effect in conjunction with atoms adsorbed into pores accounts for the porous increase of effective surface area.

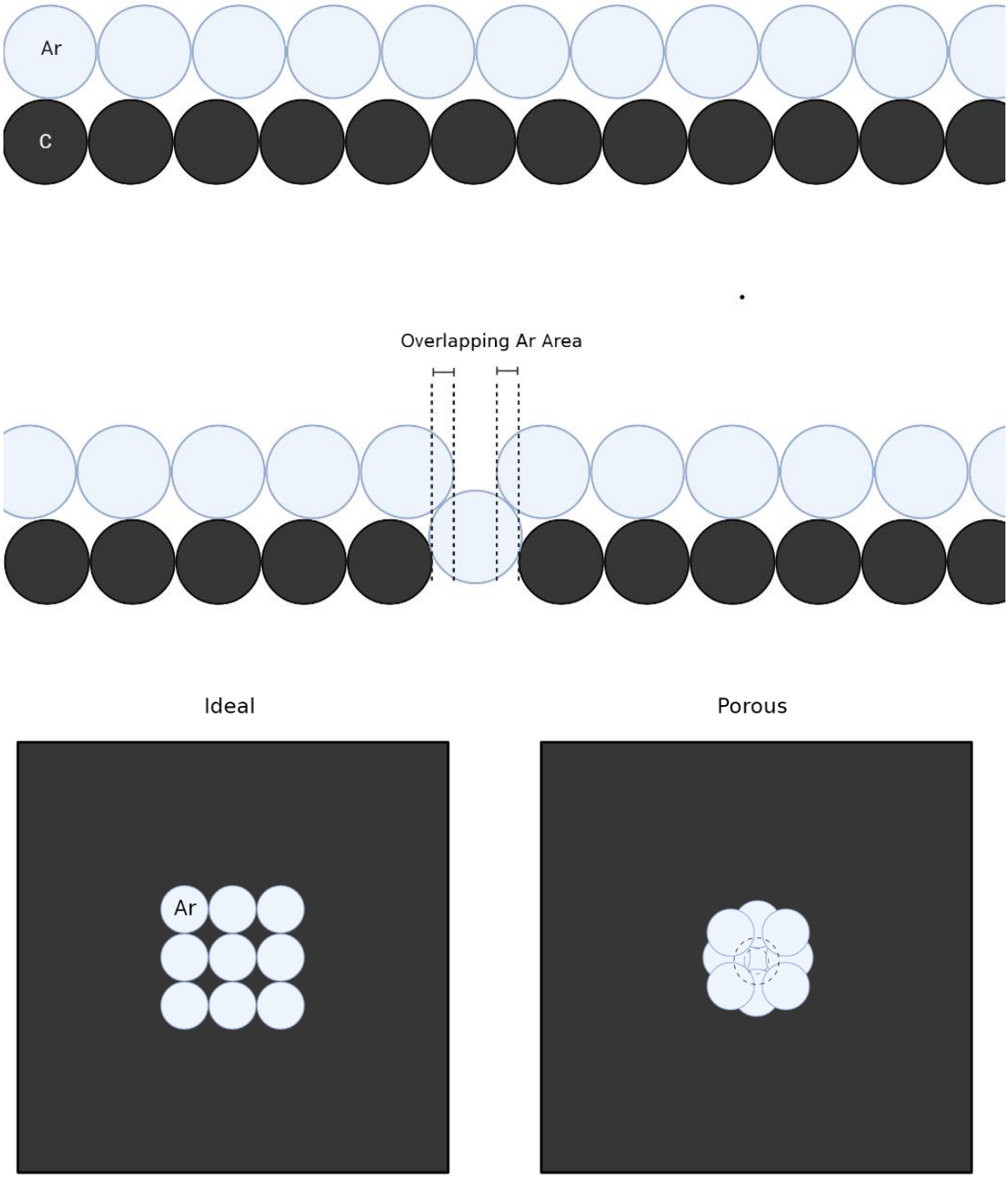

Figure 22 Ar atom sunken in pore and resulting overlapping Area

CHAPTER 7

CONCLUSIONS AND FUTURE WORK

7.1 Conclusions

This work provides Potential Energy Graphs, Specific Surface Area, and Adsorption Capacities for Nanoporous Graphene pore diameters ranging from 4.26Å to 29.2Å

It is shown that all the pore values for both geometries have higher adsorption capacity and effective specific surface area over the ideal graphene case. It is indeed possible that the specific surface area discrepancy is due to vacancy defects in experimental samples.

A portion of the increase in Argon adsorption can be attributed to the geometrical increase of surface area and Argon occupation in pore volumes. The largest contribution to specific surface area is found to be in a conical volume above the pore, as opposed to within the pore or potentially in a cylinder around the pore. This is proposed to be due to an overlap of Argon atoms with those sunken into pores.

7.2 Future Work

With regard to this proposed discrepancy resolution, an experiment can be developed to check the theory. One suggestion would be to generate graphene with a vacancy through etching, then to allow atoms to adsorb onto the surface. Then with the use of an imaging microscope one could view the formation of atoms adsorbed into and around the vacancy defective surface.

Many variables can be considered for potential energy calculations. This work focuses on pore size and pore geometry but bilayer twist angle, doping atoms and spacing are also variables that can be studied in time. Particular interest is placed on the interlayer distance where restacking effects interfere with graphene's specific surface area.

Further adsorption simulations can be done using more complicated graphene-based structures such as nanotubes and fullerenes.

Optimization of graphene electrode porosity is dependent on the electrolyte structure. Using the framework of this project, simulations can be used to determine electrolyte coverage based on pore dimensions.

Preliminary work has been done creating separation simulations using graphene nanomesh to filter a mixture of gas molecules. If more time were available this simulation could be enhanced and compared. Future work would

use these simulations to predict separation performance of nanoporous graphene filters for varied pore size and pore density.

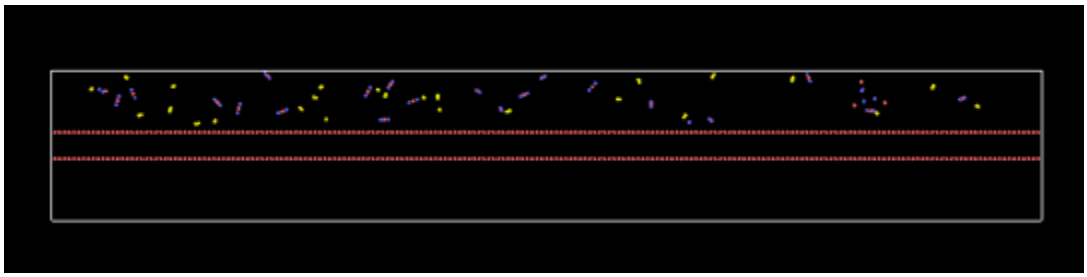

Figure 23 Preliminary snapshot of Graphene nanomesh gas separation simulation

REFERENCE LIST

[1] K.S. Novoselov, A.K. Geim, S.V. Morozov, D. Jiang, Y. Zhang, S.V. Dubonos, I.V. Grigorieva, and A.A. Firsov, "Electric Field Effect in Atomically Thin Carbon Films," Science **306**(5696), 666–669 (2004).

[2] A.K. Geim, "Graphene: Status and Prospects," Science **324**(5934), 1530–1534 (2009).

[3] A. Guirguis, J.W. Maina, X. Zhang, L.C. Henderson, L. Kong, H. Shon, and L.F. Dumée, "Applications of nano-porous graphene materials – critical review on performance and challenges," Mater. Horiz. **7**(5), 1218–1245 (2020).

[4] P. Russo, A. Hu, and G. Compagnini, "Synthesis, Properties and Potential Applications of Porous Graphene: A Review," Nano-Micro Lett. **5**(4), 260–273 (2013).

[5] S. Guo, and S. Dong, "Graphene nanosheet: synthesis, molecular engineering, thin film, hybrids, and energy and analytical applications," Chem. Soc. Rev. **40**(5), 2644–2672 (2011).

[6] H.-K. Kim, S.-M. Bak, S.W. Lee, M.-S. Kim, B. Park, S.C. Lee, Y.J. Choi, S.C. Jun, J.T. Han, K.-W. Nam, K.Y. Chung, J. Wang, J. Zhou, X.-Q. Yang, K.C. Roh, and K.-B. Kim, "Scalable fabrication of micron-scale graphene nanomeshes for high-performance supercapacitor applications," Energy Environ. Sci. **9**(4), 1270–1281 (2016).

[7] B.C. Brodie, "XIII. On the atomic weight of graphite," Philosophical Transactions of the Royal Society of London **149**, 249–259 (1997).

[8] A.T. Dideikin, and A.Y. Vul', "Graphene Oxide and Derivatives: The Place in Graphene Family," Frontiers in Physics **6**, (2019).

[9] G. Ruess, and F. Vogt, "Höchstlamellarer Kohlenstoff aus Graphitoxyhydroxyd.," Monatshefte für Chemie **78**(3), 222–242 (1948).

[10] H.P. Boehm, A. Clauss, G. Fischer, and U. Hofmann, in *Proceedings of the Fifth Conference on Carbon* (Pergamon, 1962), pp. 73–80.

[11] H.P. Boehm, R. Setton, and E. Stumpp, "Nomenclature and terminology of graphite intercalation compounds," Carbon **24**(2), 241–245 (1986).

[12] J.M. Blakely, J.S. Kim, and H.C. Potter, "Segregation of Carbon to the (100) Surface of Nickel," Journal of Applied Physics **41**(6), 2693–2697 (2003).

[13] A.M. Affoune, B.L.V. Prasad, H. Sato, T. Enoki, Y. Kaburagi, and Y. Hishiyama, "Experimental evidence of a single nano-graphene," Chemical Physics Letters **348**(1), 17–20 (2001).

[14] I. Forbeaux, J.-M. Themlin, and J.-M. Debever, "Heteroepitaxial graphite on $6H\ensuremath{-}\mathrm{SiC}(0001):$ Interface formation through conduction-band electronic structure," Phys. Rev. B **58**(24), 16396–16406 (1998).

[15] L.M. Viculis, J.J. Mack, and R.B. Kaner, "A Chemical Route to Carbon Nanoscrolls," Science **299**(5611), 1361–1361 (2003).

[16] H. Shioyama, "Cleavage of graphite to graphene," (n.d.).

[17] A.K.G. Kim Philip, "Carbon Wonderland," Scientific American, (n.d.).

[18] S. Nasir, M.Z. Hussein, Z. Zainal, and N.A. Yusof, "Carbon-Based Nanomaterials/Allotropes: A Glimpse of Their Synthesis, Properties and Some Applications," Materials (Basel) **11**(2), 295 (2018).

[19] C. Frondel, and U.B. Marvin, "Lonsdaleite, a Hexagonal Polymorph of Diamond," Nature **214**(5088), 587–589 (1967).

[20] H.W. Kroto, J.R. Heath, S.C. O'Brien, R.F. Curl, and R.E. Smalley, "C60: Buckminsterfullerene," Nature **318**(6042), 162–163 (1985).

[21] Z.-A. Liu, Y. Tao, X.-Z. Song, M. Bao, and Z. Tan, "A three dimensional N-doped graphene/CNTs/AC hybrid material for high-performance supercapacitors," RSC Advances **7**(11), 6664–6670 (2017).

[22] J. Wu, M. Wyse, D. McClain, N. Thomas, and J. Jiao, "Fabrication and Field Emission Properties of Triode-Type Carbon Nanotube Emitter Arrays," Nano Lett. **9**(2), 595–600 (2009).

[23] L. Jiang, L. Sheng, C. Long, and Z. Fan, "Densely packed graphene nanomesh-carbon nanotube hybrid film for ultra-high volumetric performance supercapacitors," Nano Energy **11**, 471–480 (2015).

[24] J.C. Meyer, A.K. Geim, M.I. Katsnelson, K.S. Novoselov, T.J. Booth, and S. Roth, "The structure of suspended graphene sheets," Nature **446**(7131), 60–63 (2007).

[25] D.G. Papageorgiou, I.A. Kinloch, and R.J. Young, "Mechanical properties of graphene and graphene-based nanocomposites," Progress in Materials Science **90**, 75–127 (2017).

[26] J.D. Mangadlao, A.C.C. de Leon, M.J.L. Felipe, and R.C. Advincula, "Electrochemical fabrication of graphene nanomesh via colloidal templating," Chem. Commun. **51**(36), 7629–7632 (2015).

[27] J.J. Yeo, Z. Liu, and T.Y. Ng, "Comparing the effects of dispersed Stone–Thrower–Wales defects and double vacancies on the thermal conductivity of graphene nanoribbons," Nanotechnology **23**(38), 385702 (2012).

[28] X. Liang, Y.-S. Jung, S. Wu, A. Ismach, D.L. Olynick, S. Cabrini, and J. Bokor, "Formation of bandgap and subbands in graphene nanomeshes with sub-10 nm ribbon width fabricated via nanoimprint lithography," Nano Lett **10**(7), 2454–2460 (2010).

[29] C. Berger, Z. Song, T. Li, X. Li, A.Y. Ogbazghi, R. Feng, Z. Dai, A.N. Marchenkov, E.H. Conrad, P.N. First, and W.A. de Heer, "Ultrathin Epitaxial Graphite: 2D Electron Gas Properties and a Route toward Graphene-based Nanoelectronics," J. Phys. Chem. B **108**(52), 19912–19916 (2004).

[30] G. Eda, G. Fanchini, and M. Chhowalla, "Large-area ultrathin films of reduced graphene oxide as a transparent and flexible electronic material," Nature Nanotech **3**(5), 270–274 (2008).

[31] N.S. Safron, M. Kim, P. Gopalan, and M.S. Arnold, "Barrier-Guided Growth of Micro- and Nano-Structured Graphene," Advanced Materials **24**(8), 1041–1045 (2012).

[32] M. Wang, L. Fu, L. Gan, C. Zhang, M. Rümmeli, A. Bachmatiuk, K. Huang, Y. Fang, and Z. Liu, "CVD Growth of Large Area Smooth-edged Graphene Nanomesh by Nanosphere Lithography," Sci Rep **3**(1), 1238 (2013).

[33] I. Jung, H. Young Jang, and S. Park, "Direct growth of graphene nanomesh using a Au nano-network as a metal catalyst via chemical vapor deposition," Appl. Phys. Lett. **103**(2), 023105 (2013).

[34] G. Ning, Z. Fan, G. Wang, J. Gao, W. Qian, and F. Wei, "Gram-scale synthesis of nanomesh graphene with high surface area and its application in supercapacitor electrodes," Chem. Commun. **47**(21), 5976–5978 (2011).

[35] C. Moreno, M. Vilas-Varela, B. Kretz, A. Garcia-Lekue, M.V. Costache, M. Paradinas, M. Panighel, G. Ceballos, S.O. Valenzuela, D. Peña, and A. Mugarza, "Bottom up synthesis of multifunctional nanoporous graphene," Science **360**(6385), 199–203 (2018).

[36] J. Bai, X. Zhong, S. Jiang, Y. Huang, and X. Duan, "Graphene nanomesh," Nature Nanotech **5**(3), 190–194 (2010).

[37] W. Lee, and S.-J. Park, "Porous Anodic Aluminum Oxide: Anodization and Templated Synthesis of Functional Nanostructures," Chem. Rev. **114**(15), 7487–7556 (2014).

[38] A. Sinitskii, and J.M. Tour, "Patterning Graphene through the Self-Assembled Templates: Toward Periodic Two-Dimensional Graphene Nanostructures with Semiconductor Properties," ACS Publications, (2010).

[39] Q. Zhang, X. Wan, F. Xing, L. Huang, G. Long, N. Yi, W. Ni, Z. Liu, J. Tian, and Y. Chen, "Solution-processable graphene mesh transparent electrodes for organic solar cells," Nano Res. **6**(7), 478–484 (2013).

[40] Y. Lin, K.A. Watson, J.-W. Kim, D.W. Baggett, D.C. Working, and J.W. Connell, "Bulk preparation of holey graphene via controlled catalytic oxidation," Nanoscale **5**(17), 7814 (2013).

[41] E.J. Radich, and P.V. Kamat, "Making Graphene Holey. Gold-Nanoparticle-Mediated Hydroxyl Radical Attack on Reduced Graphene Oxide," ACS Nano **7**(6), 5546–5557 (2013).

[42] H.C. Schniepp, J.-L. Li, M.J. McAllister, H. Sai, M. Herrera-Alonso, D.H. Adamson, R.K. Prud'homme, R. Car, D.A. Saville, and I.A. Aksay, "Functionalized Single Graphene Sheets Derived from Splitting Graphite Oxide," J. Phys. Chem. B **110**(17), 8535–8539 (2006).

[43] X. Han, M.R. Funk, F. Shen, Y.-C. Chen, Y. Li, C.J. Campbell, J. Dai, X. Yang, J.-W. Kim, Y. Liao, J.W. Connell, V. Barone, Z. Chen, Y. Lin, and L. Hu, "Scalable Holey Graphene Synthesis and Dense Electrode Fabrication toward High-Performance Ultracapacitors," ACS Nano **8**(8), 8255–8265 (2014).

[44] S.P. Koenig, L. Wang, J. Pellegrino, and J.S. Bunch, "Selective molecular sieving through porous graphene," Nature Nanotech **7**(11), 728–732 (2012).

[45] K. Sint, B. Wang, and P. Král, "Selective Ion Passage through Functionalized Graphene Nanopores," J. Am. Chem. Soc. **130**(49), 16448–16449 (2008).

[46] D. Jiang, V.R. Cooper, and S. Dai, "Porous Graphene as the Ultimate Membrane for Gas Separation," Nano Lett. **9**(12), 4019–4024 (2009).

[47] H. Liu, S. Dai, and D. Jiang, "Insights into CO2/N2 separation through nanoporous graphene from molecular dynamics," Nanoscale **5**(20), 9984–9987 (2013).

[48] H. Li, Z. Song, X. Zhang, Y. Huang, S. Li, Y. Mao, H.J. Ploehn, Y. Bao, and M. Yu, "Ultrathin, Molecular-Sieving Graphene Oxide Membranes for Selective Hydrogen Separation," Science **342**(6154), 95–98 (2013).

[49] S. Huang, M. Dakhchoune, W. Luo, E. Oveisi, G. He, M. Rezaei, J. Zhao, D.T.L. Alexander, A. Züttel, M.S. Strano, and K.V. Agrawal, "Single-layer graphene membranes by crack-free transfer for gas mixture separation," Nat Commun **9**(1), 2632 (2018).

[50] J.R. Werber, C.O. Osuji, and M. Elimelech, "Materials for next-generation desalination and water purification membranes," Nat Rev Mater **1**(5), 1–15 (2016).

[51] S.C. O'Hern, C.A. Stewart, M.S.H. Boutilier, J.-C. Idrobo, S. Bhaviripudi, S.K. Das, J. Kong, T. Laoui, M. Atieh, and R. Karnik, "Selective Molecular Transport through Intrinsic Defects in a Single Layer of CVD Graphene," ACS Nano **6**(11), 10130–10138 (2012).

[52] S.P. Surwade, S.N. Smirnov, I.V. Vlassiouk, R.R. Unocic, G.M. Veith, S. Dai, and S.M. Mahurin, "Water desalination using nanoporous single-layer graphene," Nat Nanotechnol **10**(5), 459–464 (2015).

[53] D. Cohen-Tanugi, and J.C. Grossman, "Water Desalination across Nanoporous Graphene," Nano Lett. **12**(7), 3602–3608 (2012).

[54] C.A. Merchant, K. Healy, M. Wanunu, V. Ray, N. Peterman, J. Bartel, M.D. Fischbein, K. Venta, Z. Luo, A.T.C. Johnson, and M. Drndić, "DNA translocation through graphene nanopores," Nano Lett **10**(8), 2915–2921 (2010).

[55] B.M. Venkatesan, and R. Bashir, "Nanopore sensors for nucleic acid analysis," Nature Nanotech **6**(10), 615–624 (2011).

[56] D.B. Wells, M. Belkin, J. Comer, and A. Aksimentiev, "Assessing Graphene Nanopores for Sequencing DNA," Nano Lett **12**(8), 4117–4123 (2012).

[57] F. Schedin, A.K. Geim, S.V. Morozov, E.W. Hill, P. Blake, M.I. Katsnelson, and K.S. Novoselov, "Detection of individual gas molecules adsorbed on graphene," Nat Mater **6**(9), 652–655 (2007).

[58] J. Zhang, H. Song, D. Zeng, H. Wang, Z. Qin, K. Xu, A. Pang, and C. Xie, "Facile synthesis of diverse graphene nanomeshes based on simultaneous regulation of pore size and surface structure," Sci Rep **6**(1), 32310 (2016).

[59] R.K. Paul, S. Badhulika, N.M. Saucedo, and A. Mulchandani, "Graphene Nanomesh As Highly Sensitive Chemiresistor Gas Sensor," Anal. Chem. **84**(19), 8171–8178 (2012).

[60] J. Li, and M. Östling, "Prevention of Graphene Restacking for Performance Boost of Supercapacitors—A Review," Crystals **3**(1), 163–190 (2013).

[61] Y. Chen, X. Zhang, D. Zhang, P. Yu, and Y. Ma, "High performance supercapacitors based on reduced graphene oxide in aqueous and ionic liquid electrolytes," Carbon **49**(2), 573–580 (2011).

[62] M. Wang, J. Yang, S. Liu, M. Li, C. Hu, and J. Qiu, "Nitrogen-doped hierarchically porous carbon nanosheets derived from polymer/graphene oxide hydrogels for high-performance supercapacitors," Journal of Colloid and Interface Science **560**, 69–76 (2020).

[63] J. Xiao, D. Mei, X. Li, W. Xu, D. Wang, G.L. Graff, W.D. Bennett, Z. Nie, L.V. Saraf, I.A. Aksay, J. Liu, and J.-G. Zhang, "Hierarchically Porous Graphene as a Lithium–Air Battery Electrode," Nano Lett. **11**(11), 5071–5078 (2011).

[64] K. He, X. Bi, Y. Yuan, T. Foroozan, B. Song, K. Amine, J. Lu, and R. Shahbazian-Yassar, "Operando liquid cell electron microscopy of discharge and charge kinetics in lithium-oxygen batteries," Nano Energy **49**, 338–345 (2018).

[65] Y. Lin, B. Moitoso, C. Martinez-Martinez, E.D. Walsh, S.D. Lacey, J.-W. Kim, L. Dai, L. Hu, and J.W. Connell, "Ultrahigh-Capacity Lithium–Oxygen Batteries Enabled by Dry-Pressed Holey Graphene Air Cathodes," Nano Lett. **17**(5), 3252–3260 (2017).

[66] M.-Q. Zhao, Q. Zhang, J.-Q. Huang, G.-L. Tian, J.-Q. Nie, H.-J. Peng, and F. Wei, "Unstacked double-layer templated graphene for high-rate lithium–sulphur batteries," Nat Commun **5**(1), 3410 (2014).

[67] M. Thommes, "Physical Adsorption Characterization of Nanoporous Materials," Chemie Ingenieur Technik **82**(7), 1059–1073 (2010).

[68] A.K. Rappe, C.J. Casewit, K.S. Colwell, W.A. Goddard, and W.M. Skiff, "UFF, a full periodic table force field for molecular mechanics and molecular dynamics simulations," J. Am. Chem. Soc. **114**(25), 10024–10035 (1992).

[69] M.S.A. Perera, P.G. Ranjith, S.K. Choi, D. Airey, and P. Weniger, "Estimation of Gas Adsorption Capacity in Coal: A Review and an Analytical Study," International Journal of Coal Preparation and Utilization **32**(1), 25–55 (2012).

[70] A.P. Thompson, H.M. Aktulga, R. Berger, D.S. Bolintineanu, W.M. Brown, P.S. Crozier, P.J. in 't Veld, A. Kohlmeyer, S.G. Moore, T.D. Nguyen, R. Shan, M.J. Stevens, J. Tranchida, C. Trott, and S.J. Plimpton, "LAMMPS - a flexible simulation tool for particle-based materials modeling at the atomic, meso, and continuum scales," Computer Physics Communications **271**, 108171 (2022).

[71] S.O. Amrouche, D. Rekioua, and T. Rekioua, in *2015 3rd International Renewable and Sustainable Energy Conference (IRSEC)* (IEEE, Marrakech, France, 2015), pp. 1–6.

[72] A. Schneuwly, and R. Gallay, in (2000).

[73] A. Nimbalkar, and H. Kim, "Opportunities and Challenges in Twisted Bilayer Graphene: A Review," Nano-Micro Lett. **12**(1), 126 (2020).

[74] T. Khandaker, M.S. Hossain, P.K. Dhar, Md.S. Rahman, Md.A. Hossain, and M.B. Ahmed, "Efficacies of Carbon-Based Adsorbents for Carbon Dioxide Capture," Processes **8**(6), 654 (2020).

[75]"Applications of nano-porous graphene materials – critical review on performance and challenges.pdf," Google Docs, (n.d.).

[76] H. Huang, H. Shi, P. Das, J. Qin, Y. Li, X. Wang, F. Su, P. Wen, S. Li, P. Lu, F. Liu, Y. Li, Y. Zhang, Y. Wang, Z.-S. Wu, and H.-M. Cheng, "The Chemistry and Promising Applications of Graphene and Porous Graphene Materials," Advanced Functional Materials **30**(41), 1909035 (2020).

[77] T. Khandaker, M.S. Hossain, P.K. Dhar, Md.S. Rahman, Md.A. Hossain, and M.B. Ahmed, "Efficacies of Carbon-Based Adsorbents for Carbon Dioxide Capture," Processes **8**(6), 654 (2020).

[78] Z. Liu, S.-M. Zhang, J.-R. Yang, J.Z. Liu, Y.-L. Yang, and Q.-S. Zheng, "Interlayer shear strength of single crystalline graphite," Acta Mech Sin **28**(4), 978–982 (2012).

[79] K. Min, and N.R. Aluru, "Mechanical properties of graphene under shear deformation," Appl. Phys. Lett. **98**(1), 013113 (2011).

[80] A. Bosak, M. Krisch, M. Mohr, J. Maultzsch, and C. Thomsen, "Elasticity of single-crystalline graphite: Inelastic x-ray scattering study," Phys. Rev. B **75**(15), 153408 (2007).

[81] D.E. Soule, and C.W. Nezbeda, "Direct Basal-Plane Shear in Single-Crystal Graphite," Journal of Applied Physics **39**(11), 5122–5139 (1968).

[82] O.L. Blakslee, D.G. Proctor, E.J. Seldin, G.B. Spence, and T. Weng, "Elastic Constants of Compression-Annealed Pyrolytic Graphite," Journal of Applied Physics **41**(8), 3373–3382 (1970).

[83] S.R. Snyder, W.W. Gerberich, and H.S. White, "Scanning-tunneling-microscopy study of tip-induced transitions of dislocation-network structures on the surface of highly oriented pyrolytic graphite," Phys. Rev. B **47**(16), 10823–10831 (1993).

[84] M. Dienwiebel, G.S. Verhoeven, N. Pradeep, J.W.M. Frenken, J.A. Heimberg, and H.W. Zandbergen, "Superlubricity of Graphite," Phys. Rev. Lett. **92**(12), 126101 (2004).

[85] Z. Liu, J.Z. Liu, Y. Cheng, Z. Li, L. Wang, and Q. Zheng, "Interlayer binding energy of graphite: A mesoscopic determination from deformation," Phys. Rev. B **85**(20), 205418 (2012).

[86] T. Gould, Z. Liu, J.Z. Liu, J.F. Dobson, Q. Zheng, and S. Lebègue, "Binding and interlayer force in the near-contact region of two graphite slabs: Experiment and theory," J. Chem. Phys. **139**(22), 224704 (2013).

[87] C. l. Han, X. y. Yang, X. f. Shen, T. s. Peng, H. f. Cheng, F. g. Zhang, and J. x. Zhang, "Application of response surface method (RSM) to investigate the effects of process parameters on the microstructure and shear strength of TZM/graphite joints bonded by using spark plasma sintering," International Journal of Refractory Metals and Hard Materials **100**, (2021).

[88] A.I. Siahlo, A.M. Popov, N.A. Poklonski, Y.E. Lozovik, and S.A. Vyrko, "Graphene membrane-based NEMS for study of interface interaction," Physica E: Low-Dimensional Systems and Nanostructures **115**, 113645 (2020).

[89] H. Rokni, and W. Lu, "Direct measurements of interfacial adhesion in 2D materials and van der Waals heterostructures in ambient air," Nat Commun **11**(1), 5607 (2020).

[90] E. Koren, E. Lörtscher, C. Rawlings, A.W. Knoll, and U. Duerig, "Adhesion and friction in mesoscopic graphite contacts," Science, (2015).

[91] L. Ruiz, W. Xia, Z. Meng, and S. Keten, "A coarse-grained model for the mechanical behavior of multi-layer graphene," Carbon **82**, 103–115 (2015).

[92] X. Chen, F. Tian, C. Persson, W. Duan, and N. Chen, "Interlayer interactions in graphites," Sci Rep **3**(1), 3046 (2013).

[93] C.R.C. Rêgo, L.N. Oliveira, P. Tereshchuk, and J.L.F.D. Silva, "Comparative study of van der Waals corrections to the bulk properties of graphite," J. Phys.: Condens. Matter **27**(41), 415502 (2015).

[94] M. Daly, C. Cao, H. Sun, Y. Sun, T. Filleter, and C.V. Singh, "Interfacial Shear Strength of Multilayer Graphene Oxide Films," ACS Nano **10**(2), 1939–1947 (2016).

[95] K.-M. Lee, J. Jeong, Y. Lee, J. Kim, and T.-Y. Choi, "Mechanical Exfoliation Of Single Layer Graphene From Hopg At Room Atmosphere Environment," International Journal of Innovations in Engineering and Technology **10**(2), 9 (2018).

[96] R. Taylor, R.G. Brown, I. GILtZHIUST, E. Hall, A.T. HODDSf, B.T. Kelly, and F. Morris, "THE MECHANICAL PROPERTIES OF REACTOR GRAPHITE," 13 (n.d.).

[97] Y. Guo, W. Guo, and C. Chen, "Modifying atomic-scale friction between two graphene sheets: A molecular-force-field study," Phys. Rev. B **76**(15), 155429 (2007).

[98] F. Bonelli, N. Manini, E. Cadelano, and L. Colombo, "Atomistic simulations of the sliding friction of graphene flakes," Eur. Phys. J. B **70**(4), 449–459 (2009).

[99] X.D. Ding, Y.Z. Wang, X.M. Xiong, X.S. Du, and J.X. Zhang, "Measurement of shear strength for HOPG with scanning tunneling microscopy by thermal excitation method," Ultramicroscopy **115**, 1–6 (2012).

[100] A. Guirguis, J.W. Maina, X. Zhang, L.C. Henderson, L. Kong, H. Shon, and L.F. Dumée, "Applications of nano-porous graphene materials – critical review on performance and challenges," Mater. Horiz. **7**(5), 1218–1245 (2020).

[101]"Nanoporous graphene materials | Elsevier Enhanced Reader," (n.d.).

[102] Y. Lin, Y. Liao, Z. Chen, and J.W. Connell, "Holey graphene: a unique structural derivative of graphene," Materials Research Letters **5**(4), 209–234 (2017).

[103] T. Yang, H. Lin, X. Zheng, K. Ping Loh, and B. Jia, "Tailoring pores in graphene-based materials: from generation to applications," Journal of Materials Chemistry A **5**(32), 16537–16558 (2017).

[104] L. Wang, M.S.H. Boutilier, P.R. Kidambi, D. Jang, N.G. Hadjiconstantinou, and R. Karnik, "Fundamental transport mechanisms, fabrication and potential applications of nanoporous atomically thin membranes," Nature Nanotech **12**(6), 509–522 (2017).

[105] A. Guirguis, L.F. Dumée, D.J. Eyckens, M.K. Stanfield, Y. Yin, G.G. Andersson, L. Kong, and L.C. Henderson, "Size-Controlled Nanosculpture of Cylindrical Pores across Multilayer Graphene via Photocatalytic Perforation," Advanced Materials Interfaces **9**(9), 2102129 (2022).

[106] N. S. Rajput, S.A. Zadjali, M. Gutierrez, A.M. K. Esawi, and M.A. Teneiji, "Synthesis of holey graphene for advanced nanotechnological applications," RSC Advances **11**(44), 27381–27405 (2021).

[107] Y. Lin, X. Han, C.J. Campbell, J.-W. Kim, B. Zhao, W. Luo, J. Dai, L. Hu, and J.W. Connell, "Holey Graphene Nanomanufacturing: Structure, Composition, and Electrochemical Properties," Adv. Funct. Mater. **25**(19), 2920–2927 (2015).

[108] S.M. George, "Atomic Layer Deposition: An Overview," Chem. Rev. **110**(1), 111–131 (2010).

[109] W. Lee, and S.-J. Park, "Porous Anodic Aluminum Oxide: Anodization and Templated Synthesis of Functional Nanostructures," ACS Publications, (2014).

[110] Y. Lin, K.A. Watson, J.-W. Kim, D.W. Baggett, D.C. Working, and J.W. Connell, "Bulk preparation of holey graphene via controlled catalytic oxidation," Nanoscale **5**(17), 7814–7824 (2013).

[111] P. Russo, A. Hu, and G. Compagnini, "Synthesis, Properties and Potential Applications of Porous Graphene: A Review," Nano-Micro Lett. **5**(4), 260–273 (2013).

[112] J. Werber, C.O. Osuji, and M. Elimelech, "Materials for next-generation desalination and water purification membranes," Nature Reviews Materials **1**(16018), (2016).

[113] S.C. O'Hern, C.A. Stewart, M.S.H. Boutilier, J.-C. Idrobo, S. Bhaviripudi, S.K. Das, J. Kong, T. Laoui, M. Atieh, and R. Karnik, "Selective Molecular Transport through Intrinsic Defects in a Single Layer of CVD Graphene," ACS Nano **6**(11), 10130–10138 (2012).

[114] Y.-H. Zhang, Y.-B. Chen, K.-G. Zhou, C.-H. Liu, J. Zeng, H.-L. Zhang, and Y. Peng, "Improving gas sensing properties of graphene by introducing dopants and defects: a first-principles study," Nanotechnology **20**(18), 185504 (2009).

[115] G. Fagerlund, "Determination of specific surface by the BET method," Mat. Constr. **6**(3), 239–245 (1973).

[116] M. Khalfaoui, S. Knani, M.A. Hachicha, and A. Ben Lamine, "New theoretical expressions for the five adsorption type isotherms clasified by BET based on statistical physics treatment," Journal of Colloid and Interface Science **263**, 350–6 (2003).

[117] H. Swenson, and N.P. Stadie, "Langmuir's Theory of Adsorption: A Centennial Review," Langmuir **35**(16), 5409–5426 (2019).

[118] K.Y. Foo, and B.H. Hameed, "Insights into the modeling of adsorption isotherm systems," Chemical Engineering Journal **156**(1), 2–10 (2010).

[119] L. Kong, and H. Adidharma, "A new adsorption model based on generalized van der Waals partition function for the description of all types of adsorption isotherms," Chemical Engineering Journal **375**, 122112 (2019).

[120] M.A. Al-Ghouti, and D.A. Da'ana, "Guidelines for the use and interpretation of adsorption isotherm models: A review," Journal of Hazardous Materials **393**, 122383 (2020).

[121] J. Li, and M. Östling, "Prevention of Graphene Restacking for Performance Boost of Supercapacitors—A Review," Crystals **3**(1), 163–190 (2013).

[122] M.D. Stoller, S. Park, Y. Zhu, J. An, and R.S. Ruoff, "Graphene-Based Ultracapacitors," Nano Lett. **8**(10), 3498–3502 (2008).

[123] J. Chen, C. Li, and G. Shi, "Graphene Materials for Electrochemical Capacitors," J. Phys. Chem. Lett. **4**(8), 1244–1253 (2013).

[124] G. Ning, Z. Fan, G. Wang, J. Gao, W. Qian, and F. Wei, "Gram-scale synthesis of nanomesh graphene with high surface area and its application in supercapacitor electrodes," Chem. Commun. **47**(21), 5976–5978 (2011).

[125] K. Mahankali, N.K. Thangavel, Y. Ding, S.K. Putatunda, and L.M.R. Arava, "Interfacial behavior of water-in-salt electrolytes at porous electrodes and its effect on supercapacitor performance," Electrochimica Acta **326**, 134989 (2019).

[126] Y. Lin, B. Moitoso, C. Martinez-Martinez, E.D. Walsh, S.D. Lacey, J.-W. Kim, L. Dai, L. Hu, and J.W. Connell, "Ultrahigh-Capacity Lithium-Oxygen Batteries Enabled by Dry-Pressed Holey Graphene Air Cathodes," Nano Lett **17**(5), 3252–3260 (2017).

[127] C. Tang, B.-Q. Li, Q. Zhang, L. Zhu, H.-F. Wang, J.-L. Shi, and F. Wei, "CaO-Templated Growth of Hierarchical Porous Graphene for High-Power Lithium–Sulfur Battery Applications," Advanced Functional Materials **26**(4), 577–585 (2016).

[128] S.M. Fatemi, and M. Foroutan, "Recent findings about ionic liquids mixtures obtained by molecular dynamics simulation," Journal of Nanostructure in Chemistry **5**, 243–253 (2015).

[129] M. Thommes, K. Kaneko, A. Neimark, J. Olivier, F. Rodriguez-Reinoso, J. Rouquerol, and K. Sing, "Physisorption of gases, with special reference to the evaluation of surface area and pore size distribution (IUPAC Technical Report)," Pure and Applied Chemistry **87**, (2015).

[130] L. Chen, C. Batchelor-McAuley, B. Rasche, C. Johnston, N. Hindle, and R.G. Compton, "Surface area measurements of graphene and graphene oxide samples: Dopamine adsorption as a complement or alternative to methylene blue?," Applied Materials Today **18**, 100506 (2020).

[131] B. Shubha, B. Praveen, and V. Bhat, "Graphene - Calculation of Specific Surface Area," International Journal of Applied Engineering and Management Letters, 91–97 (2023).

[132] B.S. Shubha, B.M. Praveen, and V. Bhat, "Graphene - Calculation of Specific Surface Area," IJAEML, 91–97 (2023).

[133] V.B. Mohan, K. Jayaraman, and D. Bhattacharyya, "Brunauer–Emmett–Teller (BET) specific surface area analysis of different graphene materials: A comparison to their structural regularity and electrical properties," Solid State Communications **320**, 114004 (2020).

[134] N. Boulanger, A.S. Kuzenkova, A. Iakunkov, A. Nordenström, A.Yu. Romanchuk, A.L. Trigub, P.V. Zasimov, M. Prodana, M. Enachescu, S. Bauters, L. Amidani, K.O. Kvashnina, S.N. Kalmykov, and A.V. Talyzin, "High Surface Area '3D Graphene Oxide' for Enhanced Sorption of Radionuclides," Advanced Materials Interfaces **9**(18), 2200510 (2022).

[135] P. Kamedulski, M. Skorupska, P. Binkowski, W. Arendarska, A. Ilnicka, and J.P. Lukaszewicz, "High surface area micro-mesoporous graphene for electrochemical applications," Sci Rep **11**(1), 22054 (2021).

[136] F.R. Sultanov, Ch. Daulbayev, B. Bakbolat, Z.A. Mansurov, A.A. Urazgaliyeva, R. Ebrahim, S.S. Pei, and K.-P. Huang, "Microwave-enhanced chemical vapor deposition graphene nanoplatelets-derived 3D porous materials for oil/water separation," Carbon Lett. **30**(1), 81–92 (2020).

[137] Y. Zhu, S. Murali, M.D. Stoller, K.J. Ganesh, W. Cai, P.J. Ferreira, A. Pirkle, R.M. Wallace, K.A. Cychosz, M. Thommes, D. Su, E.A. Stach, and R.S. Ruoff, "Carbon-Based Supercapacitors Produced by Activation of Graphene," Science **332**(6037), 1537–1541 (2011).

[138] L. Bellucci, and V. Tozzini, "Engineering 3D Graphene-Based Materials: State of the Art and Perspectives," Molecules **25**, 339 (2020).

[139] L. Bellucci, and V. Tozzini, "Engineering 3D Graphene-Based Materials: State of the Art and Perspectives," Molecules **25**(2), 339 (2020).

[140] S. Brunauer, P.H. Emmett, and E. Teller, "Adsorption of Gases in Multimolecular Layers," J. Am. Chem. Soc. **60**(2), 309–319 (1938).

[141] D.R. Rout, H.M. Jena, O. Baigenzhenov, and A. Hosseini-Bandegharaei, "Graphene-based materials for effective adsorption of organic and inorganic pollutants: A critical and comprehensive review," Science of The Total Environment **863**, 160871 (2023).

[142] K. Karunakaran, M. Usman, and M. Sillanpää, "A Review on Superadsorbents with Adsorption Capacity ≥1000 mg g−1 and Perspectives on Their Upscaling for Water/Wastewater Treatment," Sustainability **14**(24), 16927 (2022).

[143]"Graphene based adsorbents for remediation of noxious pollutants from wastewater | Elsevier Enhanced Reader," (n.d.).

[144] N. Baig, D. Ihsanullah, M. Sajid, and T. Saleh, "Graphene-based adsorbents for the removal of toxic organic pollutants: A review," Journal of Environmental Management **244**, 370–382 (2019).

[145] M. Manyangadze, N.H.M. Chikuruwo, T.B. Narsaiah, C.S. Chakra, M. Radhakumari, and G. Danha, "Enhancing adsorption capacity of nano-adsorbents via surface modification: A review," South African Journal of Chemical Engineering **31**, 25–32 (2020).

[146] C.J. Shearer, A.D. Slattery, A.J. Stapleton, J.G. Shapter, and C.T. Gibson, "Accurate thickness measurement of graphene," Nanotechnology **27**(12), 125704 (2016).

[147] D. Akinwande, C.J. Brennan, J.S. Bunch, P. Egberts, J.R. Felts, H. Gao, R. Huang, J.-S. Kim, T. Li, Y. Li, K.M. Liechti, N. Lu, H.S. Park, E.J. Reed, P. Wang, B.I. Yakobson, T. Zhang, Y.-W. Zhang, Y. Zhou, and Y. Zhu, "A review on mechanics and mechanical properties of 2D materials—Graphene and beyond," Extreme Mechanics Letters **13**, 42–77 (2017).

[148]"Mechanical properties of graphene and graphene-based nanocomposites | Elsevier Enhanced Reader," (n.d.).

[149] E. Quesnel, F. Roux, F. Emieux, P. Faucherand, E. Kymakis, G. Volonakis, F. Giustino, B. Martín-García, I. Moreels, S.A. Gürsel, A.B. Yurtcan, V.D. Noto, A. Talyzin, I. Baburin, D. Tranca, G. Seifert, L. Crema, G. Speranza, V. Tozzini, P. Bondavalli, G. Pognon, C. Botas, D. Carriazo, G. Singh, T. Rojo, G. Kim, W. Yu, C.P. Grey, and V. Pellegrini, "Graphene-based technologies for energy applications, challenges and perspectives," 2D Mater. **2**(3), 030204 (2015).

[150] I.A. Baburin, A. Klechikov, G. Mercier, A. Talyzin, and G. Seifert, "Hydrogen adsorption by perforated graphene," International Journal of Hydrogen Energy **40**(20), 6594–6599 (2015).

[151] X. Li, Y. Chen, Z. Cheng, L. Jia, S. Mo, and Z. Liu, "Ultrahigh specific surface area of graphene for eliminating subcooling of water," Applied Energy **130**, 824–829 (2014).

[152] S. Zhang, H. Wang, J. Liu, and C. Bao, "Measuring the specific surface area of monolayer graphene oxide in water," Materials Letters **261**, 127098 (2020).

[153] M.D. Levi, L. Daikhin, D. Aurbach, and V. Presser, "Quartz Crystal Microbalance with Dissipation Monitoring (EQCM-D) for in-situ studies of electrodes for supercapacitors and batteries: A mini-review," Electrochemistry Communications **67**, 16–21 (2016).

[154] N. Shpigel, M.D. Levi, S. Sigalov, O. Girshevitz, D. Aurbach, L. Daikhin, P. Pikma, M. Marandi, A. Jänes, E. Lust, N. Jäckel, and V. Presser, "In situ hydrodynamic spectroscopy for structure characterization of porous energy storage electrodes," Nature Mater **15**(5), 570–575 (2016).

[155] K.Keiji. Kanazawa, and J.G. Gordon, "Frequency of a quartz microbalance in contact with liquid," Anal. Chem. **57**(8), 1770–1771 (1985).

[156]"[PDF] C60: Buckminsterfullerene by Harold W. Kroto, Harold W. Kroto, James R. Heath, Sean C. O'Brien, Robert F. Curl, Richard E. Smalley · 10.1038/318162a0 · OA.mg," (n.d.).

[157] L. Jiang, and Z. Fan, "Design of advanced porous graphene materials: from graphene nanomesh to 3D architectures," Nanoscale **6**(4), 1922–1945 (2014).

[158] L. Jiang, and Z. Fan, "Design of advanced porous graphene materials: from graphene nanomesh to 3D architectures," Nanoscale **6**(4), 1922–1945 (2014).

[159] P.A. Thrower, and R.M. Mayer, "Point defects and self-diffusion in graphite," Physica Status Solidi (a) **47**(1), 11–37 (1978).

[160] L. Zhu, D. Shen, and K.H. Luo, "A critical review on VOCs adsorption by different porous materials: Species, mechanisms and modification methods," Journal of Hazardous Materials **389**, 122102 (2020).

VITA

Jonathan Lee is an interdisciplinary Ph.D. candidate at the University of Missouri-Kansas City. His main discipline is Physics, and his co-discipline is Computer and Electrical Engineering. He has done experimental studies on ionic liquids and film interfaces with atomic force microscopy, quartz crystal microbalances and molecular dynamics packages. His current research areas include condensed matter physics, and material surface science.